



ALMA MATER STUDIORUM
UNIVERSITÀ DI BOLOGNA

ARCHIVIO ISTITUZIONALE
DELLA RICERCA

Alma Mater Studiorum Università di Bologna
Archivio istituzionale della ricerca

Surface deformations and gravity changes caused by pressurized finite ellipsoidal cavities

This is the final peer-reviewed author's accepted manuscript (postprint) of the following publication:

Published Version:

Surface deformations and gravity changes caused by pressurized finite ellipsoidal cavities / Nikkhoo, M; Rivalta, E. - In: GEOPHYSICAL JOURNAL INTERNATIONAL. - ISSN 0956-540X. - ELETTRONICO. - 232:1(2022), pp. 643-655. [10.1093/gji/ggac351]

Availability:

This version is available at: <https://hdl.handle.net/11585/904051> since: 2022-11-18

Published:

DOI: <http://doi.org/10.1093/gji/ggac351>

Terms of use:

Some rights reserved. The terms and conditions for the reuse of this version of the manuscript are specified in the publishing policy. For all terms of use and more information see the publisher's website.

This item was downloaded from IRIS Università di Bologna (<https://cris.unibo.it/>).
When citing, please refer to the published version.

(Article begins on next page)

This is the final peer-reviewed accepted manuscript of:

Mehdi Nikkhoo , Eleonora Rivalta, Surface deformations and gravity changes caused by pressurized finite ellipsoidal cavities, *Geophysical Journal International*, Volume 232, Issue 1, January 2023, Pages 643–655

The final published version is available online at <https://doi.org/10.1093/gji/ggac351>

Terms of use:

Some rights reserved. The terms and conditions for the reuse of this version of the manuscript are specified in the publishing policy. For all terms of use and more information see the publisher's website.

This item was downloaded from IRIS Università di Bologna (<https://cris.unibo.it/>)

When citing, please refer to the published version.



Surface deformations and gravity changes caused by pressurized finite ellipsoidal cavities

Journal:	<i>Geophysical Journal International</i>
Manuscript ID	GJI-S-22-0146L.R2
Manuscript Type:	Research Paper
Date Submitted by the Author:	30-Aug-2022
Complete List of Authors:	Nikkhoo, Mehdi; Helmholtz Centre Potsdam German Research Centre for Geosciences, Department of Geophysics; Abdus Salam International Centre for Theoretical Physics Condensed Matter and Statistical Physics Section, Earth System Physics Rivalta, Eleonora; Helmholtz Centre Potsdam German Research Centre for Geosciences, Department of Geophysics; Alma Mater Studiorum University of Bologna, Department of Physics and Astronomy "Augusto Righi"
Additional Keywords:	
Keywords:	Geomechanics < OTHER SUBJECTS, Kinematics of crustal and mantle deformation < TECTONOPHYSICS, Mechanics, theory, and modelling < TECTONOPHYSICS, Physics of magma and magma bodies < VOLCANOLOGY, Volcano monitoring < VOLCANOLOGY, Time variable gravity < GEODESY and GRAVITY

submitted to *Geophys. J. Int.*

Surface deformations and gravity changes caused by pressurized finite ellipsoidal cavities

Mehdi Nikkhoo^{1,2} and Eleonora Rivalta^{1,3}

¹ *GFZ German Research Centre for Geosciences, Potsdam, Germany. E-mail: mehdi.nikkhoo@gfz-potsdam.de*

² *The Abdus Salam International Center for Theoretical Physics, Trieste, Italy,*

³ *Department of Physics and Astronomy, Alma Mater Studiorum University of Bologna, Italy.*

SUMMARY

~~Volcano deformation monitoring is fundamental to detect pressurizations of magma bodies and forecasting any ensuing eruptions. Analytical and quasi-analytical solutions for pressurized cavities are routinely used to constrain volcano deformation sources through inversion of surface displacement data. Due to their computational efficiency, such solutions enable a thorough exploration of the parameter space and thereby provide insight into the physics of magma-rock interaction. Developing more general deformation models can help us better characterize subsurface magma storage.~~ We develop quasi-analytical solutions for the surface deformation field and gravity changes due to the pressurization of a finite (triaxial) ellipsoidal cavity in a half-space. The solution is in the form of a non-uniform distribution of triaxial point sources within the cavity. The point sources have the same aspect ratio, determined by the cavity shape, while their strengths and spacing are determined in an adaptive manner, such that the net point-source potency per unit volume is uniform. We validate and compare our solution with analytical and numerical solutions. We provide computationally-efficient MATLAB codes tailored for source inversions. This solution opens the possibility of exploring the geometry of shallow magma chambers for potential deviations from axial symmetry.

2 *Mehdi Nikkhoo, Eleonora Rivalta*

22 **Key words:** Geomechanics; Kinematics of crustal and mantle deformation; Physics of
23 magma and magma bodies; Volcano monitoring.

24 1 INTRODUCTION

25 Volcano deformation is an indicator of ongoing fluid transport or pressure build-up within magma
26 reservoirs and is often a reliable precursor to eruptions (Dvorak & Dzurisin 1997; Dzurisin 2006).
27 Pressurization of magma chambers may be caused by replenishment with new magma from below,
28 or degassing of the magma residing in the chamber (Edmonds & Woods 2018; Degruyter et al. 2019;
29 Trasatti et al. 2019; Hill et al. 2020; Wicks et al. 2020; Caricchi et al. 2021). Pressure may also build
30 up within shallow magma bodies, such as lava domes (Salzer et al. 2014; Wang & Aoki 2019), or
31 hydrothermal reservoirs due to rapid ascent of volatiles or magma-water interaction (Kobayashi et al.
32 2018; Ueda et al. 2018; Narita et al. 2020; Yunjun et al. 2021). Magma bodies may also expand, or con-
33 tract, due to thermal effects (Furuya 2004, 2005; Wang & Aoki 2019). Critically pressurized magma
34 chambers may rupture leading to injection of a magmatic dike and ensuing chamber depressuriza-
35 tion (Narita et al. 2019). These processes may generate measurable surface deformations (Dvorak &
36 Dzurisin 1997; Dzurisin 2000; Lu & Dzurisin 2014; Biggs & Pritchard 2017), which can be evaluated
37 through mathematical models to infer the source parameters: the shape, location, spatial orientation
38 and volume change (Dvorak & Dzurisin 1997; Dzurisin 2003; Lisowski 2007; Segall 2010). Such
39 analyses have immensely contributed to our understanding of volcanic processes (Dvorak & Dzurisin
40 1997; Dzurisin 2006; Segall 2010). This has motivated both advancing the technologies for acquiring
41 deformation data with higher spatio-temporal resolutions (Pinel et al. 2014; Poland & Zebker 2022),
42 and developing new analytical and numerical deformation source models (Amoruso & Crescentini
43 2011; Segall 2016; Nikkhoo et al. 2017).

44 Analytical or quasi-analytical source models, which are fast to compute and need no expert set-
45 up, are key assets for these inversions during volcanic crises (Beauducel et al. 2020a,b) or for in-depth
46 studies of multiple eruptive cycles over extended time periods (Amoruso et al. 2014; Lisowski et al.
47 2021; Bruno et al. 2022). This has motivated the development of several new analytical source inver-
48 sion software packages (Battaglia et al. 2013; Bagnardi & Hooper 2018; Cannavó 2019; Beauducel
49 et al. 2020a; Heimann et al. 2019; Vasyura-Bathke et al. 2019, 2020; Trasatti 2022). Moreover, ana-
50 lytical solutions can be used as components of both data assimilation frameworks (Bato et al. 2017;
51 Zhan et al. 2017) and physical volcano deformation models describing the evolution of the plumb-
52 ing systems (Anderson & Segall 2011, 2013; Anderson & Poland 2016). New generalized analytical
53 solutions would offer more flexibility for all these applications.

1
2
3
4
5
6 54 The surface displacements caused by deep volumetric deformation sources can be adequately
7 55 modelled through point-source models such as the point spherical (Mogi 1958), point spheroidal
8 56 (Davis et al. 1974) and point ellipsoidal (Davis 1986) models. A triaxial point-source model that
9 57 includes the mentioned solutions as special cases is the point Compound Dislocation Model (point
10 58 CDM; Nikkhoo et al. 2017).

11
12
13
14 59 McTigue (1987) and Yang et al. (1988) showed that point sources (Mogi (1958) and Davis (1986)
15 60 models, respectively) fail to properly simulate the near-field surface displacements associated with
16 61 shallow pressurized cavities if the depth to semi-major axis ratio of the cavity is smaller than 2. In the
17 62 case of pressurized penny-shaped cracks, a point tensile dislocation can adequately simulate the near-
18 63 field surface displacements if the depth to semi-major axis ratio is greater than 5 (Sun 1969; Fialko
19 64 et al. 2001). This is because the near-field displacements are affected by the finite dimension of the
20 65 source. For such cases, finite source models are required to constrain all source parameters reliably
21 66 (Lisowski 2007; Segall 2010). The most commonly-used finite source models of uniform pressure are
22 67 the finite spherical (McTigue 1987), finite spheroidal (Yang et al. 1988) and penny-shaped crack (Sun
23 68 1969; Fialko et al. 2001) models. As these models are all axisymmetric, they cannot properly represent
24 69 the deformation field caused by triaxial sources.

25
26
27
28
29
30
31 70 After Eshelby (1957), a solution for a uniformly pressurized finite ellipsoidal cavity in the full
32 71 space can be obtained by appropriate triaxial point sources uniformly distributed throughout the cavity
33 72 (Yang et al. 1988; Segall 2010). Davis et al. (1974) and Davis (1986) incorporated the Mindlin (1936)
34 73 half-space Green's functions instead of the full-space Green's functions into the Eshelby's solution,
35 74 a procedure that we call below the "Davis approximation", to derive their approximate half-space
36 75 point-source solution. Similarly, Yang et al. (1988) used the Davis approximation to develop a closed-
37 76 form, approximate solution for finite prolate spheroids. Cervelli (2013) extended the Yang et al. (1988)
38 77 solution to a model for both prolate and oblate spheroids. Yang et al. (1988) also showed for vertical
39 78 prolate spheroids that, as a rule of thumb, the solution is fairly accurate if the depth to the top of the
40 79 spheroid is larger than the radius of curvature at the spheroid top.

41
42
43
44
45
46
47
48 80 Amoruso & Crescentini (2011) proposed a multipole expansion up to quadrupole terms of the
49 81 Eshelby (1957) solution as a finite-source model for pressurized triaxial ellipsoids—the closed-form
50 82 analytical expression of this model were provided later by Amoruso & Crescentini (2013). Moreover,
51 83 Amoruso & Crescentini (2011) developed a configuration composed of 7 triaxial point sources (Davis
52 84 1986) of appropriate strength and location (one source at the center and six sources located symmet-
53 85 rically on the axes of the ellipsoidal cavity). They showed that the 7-point source solution is in good
54 86 agreement with the closed-form analytical version of their model. Amoruso & Crescentini (2011) also
55 87 compared the 7-point-source model with the Davis (1986), McTigue (1987), Yang et al. (1988) and
56
57
58
59
60

4 *Mehdi Nikkhoo, Eleonora Rivalta*

88 Fialko et al. (2001) models. However, the comparisons did not explore a wide range of source param-
89 eters, especially for shallow sources. To our knowledge, the Amoruso & Crescentini (2013) analytical
90 solution has been compared only with the 7-point-source solution, and only for 3 cavities with d_C/a_C
91 of 1.88 and 3.75 (see supporting information in Amoruso & Crescentini 2011). Thus, the range of
92 applicability of the Amoruso & Crescentini (2011) and Amoruso & Crescentini (2013) models is not
93 clear. At present, solutions properly-validated for shallow ellipsoidal sources along with computer
94 programs suitable for inversions are yet to be developed and adopted by the community.

95 In principle, it is straightforward to follow Eshelby (1957) and use the Davis approximation to
96 derive a half-space solution for finite ellipsoids in the form of an evenly-spaced distribution of triaxial
97 point sources. Amoruso et al. (2007) applied this approach to simulate the surface displacements of a
98 finite horizontal penny-shaped crack, showing that the solution is accurate if the depth-to-radius ratio
99 is larger than 0.8. However, there are at least two issues with this approach when generic finite triaxial
100 sources are considered. First, the spacing between the point sources needs to be chosen carefully such
101 that accurate results are achieved within reasonable computation times, which are imposed by the
102 application type. Specifically, rapid inversions require a large number of forward calculations to be
103 performed within a few hours or in a day—this narrows down the acceptable computation time for a
104 single forward simulation to a few seconds. The second issue is that the optimal point-source spacing
105 should be defined in a fully automatic way for any cavity geometry and accuracy requirement. This is
106 because it is plausible that the optimal spacing depends on the aspect ratio, orientation and depth of
107 the cavity. Adopting the same small spacing for all cavity geometries, or requiring the user to adapt
108 spacing to each geometry explored during the inversion, would be inefficient or even impractical.

109 Here we propose that a solution for the surface displacements associated with finite cavities can be
110 developed in the form of a non-uniform distribution of point sources (here point CDMs) with depth-
111 dependent spacing and strengths. This way, fewer, but larger magnitude, point sources are distributed
112 at deeper locations within the cavity. We first introduce an adaptive algorithm that involves a set of
113 analytical solutions controlling the location, spacing and strengths of the point CDMs. Next, we com-
114 pare our solutions with published results from analytical and numerical models. Finally, we discuss the
115 advantages, limitations and the implications of the new solution for inversions involving deformation
116 data as well as joint inversions of deformations and gravity changes.

117 2 METHODS

118 2.1 A new adaptive configuration

119 In the following we develop a solution for uniformly pressurized ellipsoidal cavities in a homogeneous,
 120 linear, elastic half-space with Poisson's ratio, ν , and bulk modulus, K . We refer to this solution as
 121 the finite Ellipsoidal Cavity Model (finite ECM). We adopt a Cartesian right-handed xyz coordinate
 122 system with the origin on the free surface and the z axis pointing upward. The parameters defining
 123 a finite ECM are: the coordinates of its center $(x_0, y_0, -d_C)$, where d_C is the depth to the center of
 124 the cavity, the semiaxes (a_x, a_y, a_z) , the rotation angles $(\omega_x, \omega_y, \omega_z)$ and the overpressure δp . If the
 125 rotation angles are zero, a_x, a_y and a_z are aligned with the x, y and z axes, respectively.

126 To implement the solution based on the the Eshelby (1957) and the Davis approximation, we
 127 distribute within the cavity a set of expanding triaxial point sources. Such triaxial point sources can
 128 be formed as a superposition of three mutually orthogonal force dipoles (Mindlin 1936; Davis 1986),
 129 or alternatively, three mutually orthogonal point tensile dislocations (Lisowski et al. 2008; Bonafede
 130 & Ferrari 2009). Here we employ the point CDM (Nikkhoo et al. 2017), which implements the latter
 131 configuration. The potencies of the three individual point dislocations (the product of opening and
 132 surface area) define the aspect ratio and the strength of the point CDM.

133 The far-field deformations due to any ellipsoidal cavity can be represented by a point CDM located
 134 at the cavity center and having potencies

$$135 \begin{pmatrix} \Delta V_x \\ \Delta V_y \\ \Delta V_z \end{pmatrix} = \frac{-V\delta p}{3K} (\mathbf{S} - \mathbf{I}_3)^{-1} \begin{pmatrix} 1 \\ 1 \\ 1 \end{pmatrix}, \quad (1)$$

136 where $V = \frac{4\pi}{3} a_x a_y a_z$ is the volume of the cavity, \mathbf{I}_3 is the identity matrix and

$$137 \mathbf{S} = \begin{pmatrix} S_{1111} & S_{1122} & S_{1133} \\ S_{2211} & S_{2222} & S_{2233} \\ S_{3311} & S_{3322} & S_{3333} \end{pmatrix},$$

138 where S_{ijjj} are the Eshelby (1957) tensor components, with the indices 1, 2 and 3 indicating the
 139 x, y and z directions, respectively (Nikkhoo et al. 2017). The terms S_{ijjj} are nonlinear functions of
 140 a_x, a_y, a_z and ν (see Eshelby 1957; Amoruso & Crescentini 2009; Segall 2010). Let a_C denote the
 141 characteristic dimension (semi-major axis) of the cavity:

$$142 a_C = \max\{a_x, a_y, a_z\}. \quad (2)$$

143 The point-source approximation is accurate if the distance between the cavity and the observation
 144 points—here d_C —is much larger than a_C (Sun 1969; McTigue 1987; Fialko et al. 2001; Segall 2010).

6 Mehdi Nikkhoo, Eleonora Rivalta

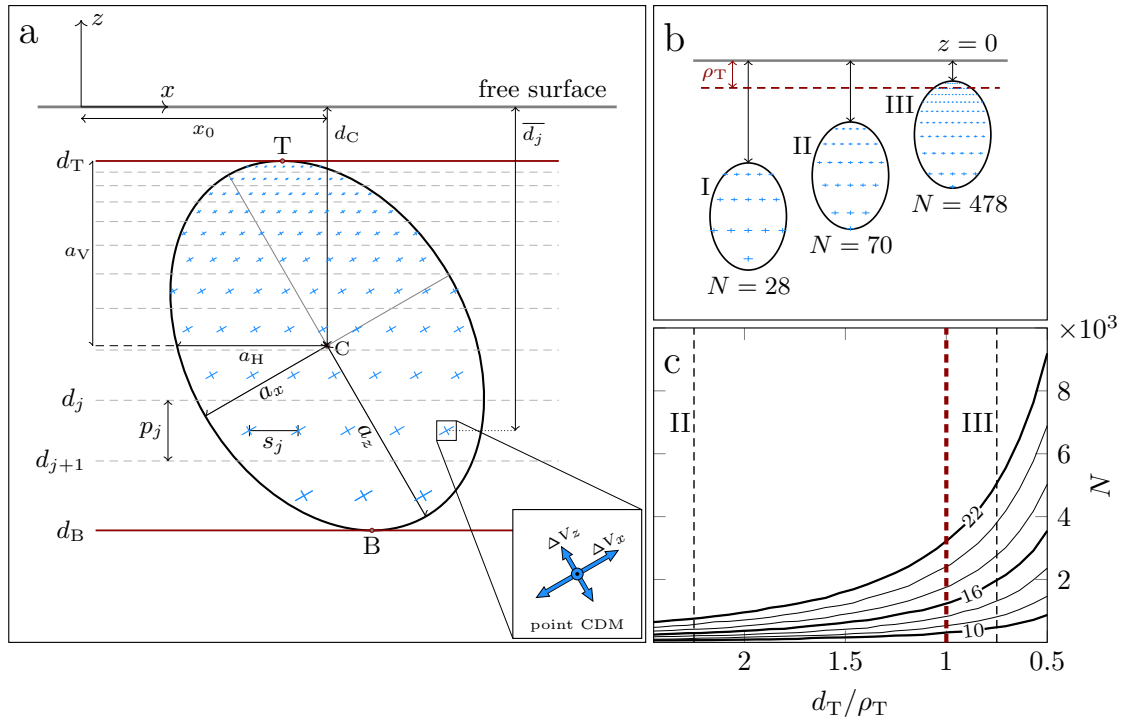


Figure 1. a) The adaptive source model for $c_r^* = 10$. The ellipsoid parameters are: center at $(x_0, 0, -d_C)$, $a_x/a_z = 0.714$, $a_z/d_C = 0.826$, $\omega_x = \omega_z = 0^\circ$ and $\omega_y = 30^\circ$. d_T and d_B are the depths to the ellipsoid top (T) and bottom (B), respectively. $d_T/d_C = 0.226$ and $d_B/d_C = 1.774$. Red lines: uppermost and lowermost partitioning planes. The j -th partition is bounded by the ellipsoid and partitioning planes (dashed lines) at depths d_j and d_{j+1} . Cross symbols are the point CDMs, with a total number $N = 879$. Inset: point CDM configuration. For this ellipsoid geometry and for $\nu = 0.25$, $\Delta V_z/\Delta V_x = 0.671$. b) Adaptive source model ($c_r^* = 10$) for the same ellipsoid as in a) but with $\omega_x = \omega_y = \omega_z = 0^\circ$. a_z/d_C is 0.344, 0.466 and 0.724 for I, II and III, respectively. d_T/ρ_T is 3.75, 2.25 and 0.85 for I, II and III, respectively. c) For the same source geometry as in panel b), the solid curves show N , for c_r^* varying between 10 and 22, as a function of d_T/ρ_T . Numbers on the thick curves indicate c_r^* . The vertical dashed line is $d_T = \rho_T$, which represents the Yang et al. (1988) rule of thumb. Note that for the tilted cavity in a) $\rho_T/a_z = 0.620$, whereas for the cavities in b) we have $\rho_T/a_z = 0.510$.

The approximation error is, thus, a function of the ratio

$$c_r = \frac{d_C}{a_C}. \quad (3)$$

Following Eshelby (1957), the near-field deformations of a finite ellipsoidal cavity can be represented by a set of point CDMs—with potencies proportional to those in equation 1—continuously distributed throughout the cavity. Each point CDM of the set can be interpreted as an “auxiliary ellipsoid”, that is, an infinitesimal ellipsoidal cavity with the same aspect ratio, pressure and spatial orientation as the finite cavity. In practice, a finite number of point CDMs can approximate the near-field solution with arbitrary accuracy. By trial and error we found that satisfactory results are achieved

1
2
3
4
5
6 153 if: 1) the point CDM spacing is such that the auxiliary ellipsoids are regularly packed (ellipsoids tan-
7 154 gent to each other at the tips of their axes), and 2) the c_r s associated with the auxiliary ellipsoids are
8
9 155 larger than a certain threshold, c_r^* , which we refer to as the “grid-spacing parameter” (section 2.3).
10 156 Thus, if the semi-axes of the auxiliary ellipsoids are $a'_x = ka_x$, $a'_y = ka_y$, $a'_z = ka_z$, where $k < 1$
11
12 157 is a scale factor, the spacing between the point CDMs in the three directions becomes $2ka_x$, $2ka_y$,
13
14 158 $2ka_z$, respectively. Denoting the depth to the top and bottom of the ellipsoidal cavity with d_T and d_B ,
15
16 159 respectively, and defining

$$17 \quad a_V = (d_B - d_T)/2, \quad (4)$$

18
19 161 as half of the vertical extent of the cavity (see Fig. 1a), the c_r for the shallowest auxiliary ellipsoid will
20
21 162 be

$$22 \quad c'_r = \frac{d'_C}{a'_C} = \frac{d_T + ka_V}{ka_C}, \quad (5)$$

23
24 164 where d'_C and a'_C are the depth to the center and semi-major axis of the shallowest auxiliary ellipsoid,
25
26 165 respectively. We note that $2a_V$ is the vertical extent of the cavity and $2ka_V$ is the vertical extent of the
27
28 166 auxiliary ellipsoids. For a given c_r^* , equation 5 can be solved for k , which determines the point CDM
29
30 167 spacing. The potencies of the point CDMs in this configuration are $(\Delta V_x/N, \Delta V_y/N, \Delta V_z/N)$, where
31
32 168 ΔV_x , ΔV_y and ΔV_z are calculated from equation 1 and N is the total number of the point CDMs.
33
34 169 Numerical convergence tests show that $c_r^* \approx 10$ provides very good results (see section 2.3), but it
35
36 170 may lead to a large N and thus, long computation times.

37
38 171 To address this problem, we have devised a new configuration in which the size of the auxiliary el-
39
40 172 llioids increases with depth such that they all have the same c_r . In this new configuration the auxiliary
41
42 173 ellipsoids are regularly packed in horizontal layers stacked on top of each other. The vertical extent
43
44 174 of the layers—that is, the vertical extent of the auxiliary ellipsoids—are obtained from top to bottom
45
46 175 through an iterative procedure. Assuming $c'_r = c_r^*$, from equation 5 we calculate the scale factor for
47
48 176 the auxiliary ellipsoids on the top layer as

$$49 \quad k_1 = d_T/(c_r^* a_C - a_V), \quad (6)$$

50
51 178 from which the vertical extent of the first layer can be calculated as $2k_1 a_V$. The depth to the top of the
52
53 179 second layer is then

$$54 \quad d_2 = d_T(1 + 1/n_p), \quad (7)$$

55
56 181 where

$$57 \quad n_p = d_T/(2k_1 a_V). \quad (8)$$

58
59 183 Using d_2 in place of d_T , and the same c_r^* , in equation 5, we determine k_2 and thus, the vertical extent of
60
61 184 the second layer. By repeating this procedure, we determine the depths, and thus the vertical extents,

8 *Mehdi Nikkhoo, Eleonora Rivalta*

of further layers. Now we determine the point CDM spacing and potencies in each layer. Let a_H and a_h denote the semi-major axis and semi-minor axis, respectively, of the horizontal ellipse formed by the intersection of the ellipsoidal cavity and a horizontal plane passing through the cavity center. The spacing of the point CDMs in the j -th layer will be $2k_j a_H$ and $2k_j a_h$ in the directions parallel to a_H and a_h , respectively. Finally, we adjust the point CDM potencies in each layer such that the potency per unit volume remains uniform throughout the cavity.

The new configuration is obtained through the following adaptive algorithm:

1. We set c_T^* depending on the desired accuracy or the maximum total number of allowed point CDMs, N_{\max} .
2. We determine d_T and d_B analytically (Appendix A) and then calculate n_p from equation 8.
3. We partition the cavity by using the planes $z = -d_T$, $z = -d_B$ and $z = -d_j$, where $d_j = d_T (1 + 1/n_p)^{j-1}$, $j = 2, 3, \dots, M - 1$ (dashed lines in Fig. 1a) in which M is the number of partitioning planes.
4. We calculate the volumes V_j of the cavity partitions analytically (see Appendix B).
5. We determine analytically the ellipses formed by the intersections of the cavity and the planes $z = -\bar{d}_j = -(d_j + d_{j+1})/2$ passing through the middle of the partitions (see Fig. 1a and Appendix C).
6. On every intersection ellipse we create a regular grid of point CDMs such that one point CDM lies at the center of the ellipse (Fig. 1a). As the grid spacing parallel to a_H and a_h we use $s_j^H = 2k_j a_H$ and $s_j^h = 2k_j a_h$, respectively, where $k_j = d_j / (c_T^* a_C - a_V)$. N_j and N denote the total number of point CDMs within the j -th partition and within the cavity, respectively. Note that every partition will contain at least one point CDM at its center.
7. For the top and bottom partitions, we calculate h'_i , for $i = 1, \dots, N_j$, as the vertical distance between each point CDM and the cavity surface.
8. We set the potencies of the point CDMs as $(\alpha_{ij} \frac{V_j}{V} \Delta V_x, \alpha_{ij} \frac{V_j}{V} \Delta V_y, \alpha_{ij} \frac{V_j}{V} \Delta V_z)$, where for the top and bottom partitions ($j = 1$ and $j = M - 1$) $\alpha_{ij} = h_i / \sum_{k=1}^{N_j} h_k$ in which $h_i = h'_i + k_j a_V$, and for all the other partitions $\alpha_{ij} = 1/N_j$.
9. We calculate the volume change, δV , associated with the finite ECM from the Eshelby (1957) solution. The calculated volume change corresponds to a pressurized cavity in full space (see section 4.3).
10. We calculate d_T/ρ_T^{\max} and d_T/ρ_T^{\min} , where ρ_T^{\max} and ρ_T^{\min} are the maximum and minimum radii of curvature at T, respectively (Appendix D). Later, we consider d_T/ρ_T^{\max} and d_C/a_C of the cavity for further assessment of the solution quality.

2.2 Computational efficiency of the finite ECM

The computation time associated with the finite ECM depends on N . For a specific c_T^* in the adaptive algorithm, N is determined by the shape (aspect ratio and size), depth and spatial orientation of the cavity (Fig. 1a-c). The non-linear link between the cavity depth and N can be better appreciated in Fig. 1b-c, where a varying depth for cavities of the same shape and orientation leads to different values for N . As the source gets very shallow, N becomes very large. However, we have to keep in mind that, similar to the Yang et al. (1988) solution, the accuracy of the finite ECM degrades if the source is too shallow. Thus, by applying some source-quality criteria, very large values for N can be automatically excluded. According to Yang et al. (1988), $d_T \gtrsim \rho_T$ defines, as a rule of thumb, a minimum depth for vertical prolate cavities (cavity top below the dashed line in Fig 1b). For such cavities, N does not exceed a few thousands, even for $c_T^* = 22$ (left-hand side of the red dashed line in Fig 1c), which is much larger than needed for an excellent solution (Section 2.3).

Once c_T^* is fixed in the adaptive algorithm, the shallower the cavity, the higher the computational efficiency achieved by using the adaptive configuration in comparison with an evenly-spaced configuration. For example for the cavity in Fig 1a, the N for the evenly-spaced configuration of equivalent accuracy is 21.5 times larger than the N for the adaptive configuration. Similar factors calculated for the first (I), second (II) and third (III) cavities in Fig 1b are 1, 2.7, 14.4, respectively. For a given c_T^* , N also depends on the other source parameters beside the cavity depth.

The finite ECM involves computing the surface displacements for N point CDMs on the same grid of observation points. Thus, similar to Beauducel et al. (2020b), we achieved further computational efficiency through a full vectorization of the original point CDM computer codes. From experimenting with the codes, we verified that the computation time associated with the finite ECM scales roughly linearly with the number of point CDMs. As an example, the computation of surface displacements at 100 observation points caused by a configuration of $N = 1000$ point CDMs requires 0.12 seconds on a personal computer (with 2.80 GHz processor with 8 threads). Similar computations for $N = 10000$ and $N = 20000$ point CDMs require 1.3 and 2.4 seconds, respectively. The adaptive algorithm along with the vectorization speed up the computation times sufficiently to render the finite ECM suitable for rapid source inversions, akin to conventional analytical solutions.

2.3 Calibration of the grid-spacing parameter

As stated earlier, the accuracy of the solution depends on c_T^* . In order to calibrate c_T^* , we use the only exact solution for finite non-spherical sources, namely, the Yang et al. (1988) solution for spheroidal cavities. We conduct systematic comparisons between the finite ECM and the Yang et al. (1988) surface displacements for ~ 7500 oblate and prolate spheroids with various aspect ratios, depths and

10 *Mehdi Nikkhoo, Eleonora Rivalta*

250 dip angles (see caption of Table 1). To do so, we calculate the surface displacements associated with
 251 the Yang et al. (1988) solution on a regular grid of points using the MATLAB codes provided by
 252 Cervelli (2013) and Battaglia et al. (2013). Next, on the same grid, we calculate the surface displacements
 253 using the finite ECM for various c_T^* . As measures of the deviation between the two solutions
 254 we calculate $\epsilon_x = \max\{(u_x^{(1)} - u_x^{(2)})/u_z^{(2)}\}$ and $\epsilon_z = \max\{(u_z^{(1)} - u_z^{(2)})/u_z^{(2)}\}$, where the “max” is
 255 calculated over all observation points, superscript “(1)” refers to the finite ECM and superscript “(2)”
 256 refers to the Yang et al. (1988) solution. We evaluate both the maximum of these deviations among
 257 all models, and the fraction of models where ϵ_x and ϵ_z are below 0.01. In order to avoid errors due to
 258 normalizing by near-zero vertical displacements, we limit the calculation to observation points with
 259 a vertical displacement larger than 10 per cent of the maximum vertical displacement on the grid.
 260 Results confirm that already with $c_T^* = 10$ a very good accuracy (relative errors smaller than ~ 0.05)
 261 is obtained. An excellent accuracy (relative errors smaller than ~ 0.02), sufficient for most practical
 262 applications, is reached with $c_T^* = 12$ for prolate sources and $c_T^* = 14$ for oblate sources. A simi-
 263 lar analysis for triaxial ellipsoids is only possible through a convergence test. Using solutions with
 264 $c_T^* = 20$ as the benchmark, we find that setting $c_T^* = 12$ leads to an excellent accuracy (relative errors
 265 smaller than ~ 0.02) for triaxial ellipsoids (see Table 1).

266 3 COMPARISON TO PUBLISHED ANALYTICAL AND NUMERICAL SOLUTIONS

267 We compare the finite ECM with published analytical and numerical solutions. We choose source pa-
 268 rameters close to the limits of the range of applicability of the finite ECM. Unless otherwise stated, we
 269 use $c_T^* = 14$ and $N_{\max} = 4000$. Note that when comparing two solutions, displacements are commonly
 270 normalized in two different ways: method I) Both solutions normalized by the maximum vertical dis-
 271 placement of one of the solutions; method II) Each solution normalized by its own maximum vertical
 272 displacement. First, we compare the finite ECM with analytical solutions and next with numerical
 273 solutions for triaxial ellipsoids. We use normalization method I in our analytical comparisons (Fig. 2)
 274 and both normalization methods I and II in the numerical comparisons (Fig. 3). We later expand on
 275 the implications of the normalization methods.

276 For the first analytical comparison we consider the Yang et al. (1988), Amoruso & Crescentini
 277 (2011) and Amoruso & Crescentini (2013) solutions (Fig. 2a). The source in this case is a prolate
 278 spheroid with $a_x/a_z = 1/3$ and $a_z/d_C = 5/6$. Despite the rather low $d_C/a_C = 1.2$ of the cavity,
 279 the displacements from the finite ECM and Yang et al. (1988) solution are in excellent agreement. In
 280 contrast, the Amoruso & Crescentini (2011) and Amoruso & Crescentini (2013) models underestimate
 281 the near-field surface displacements by almost 20%. Comparisons similar to that illustrated in Fig. 2a

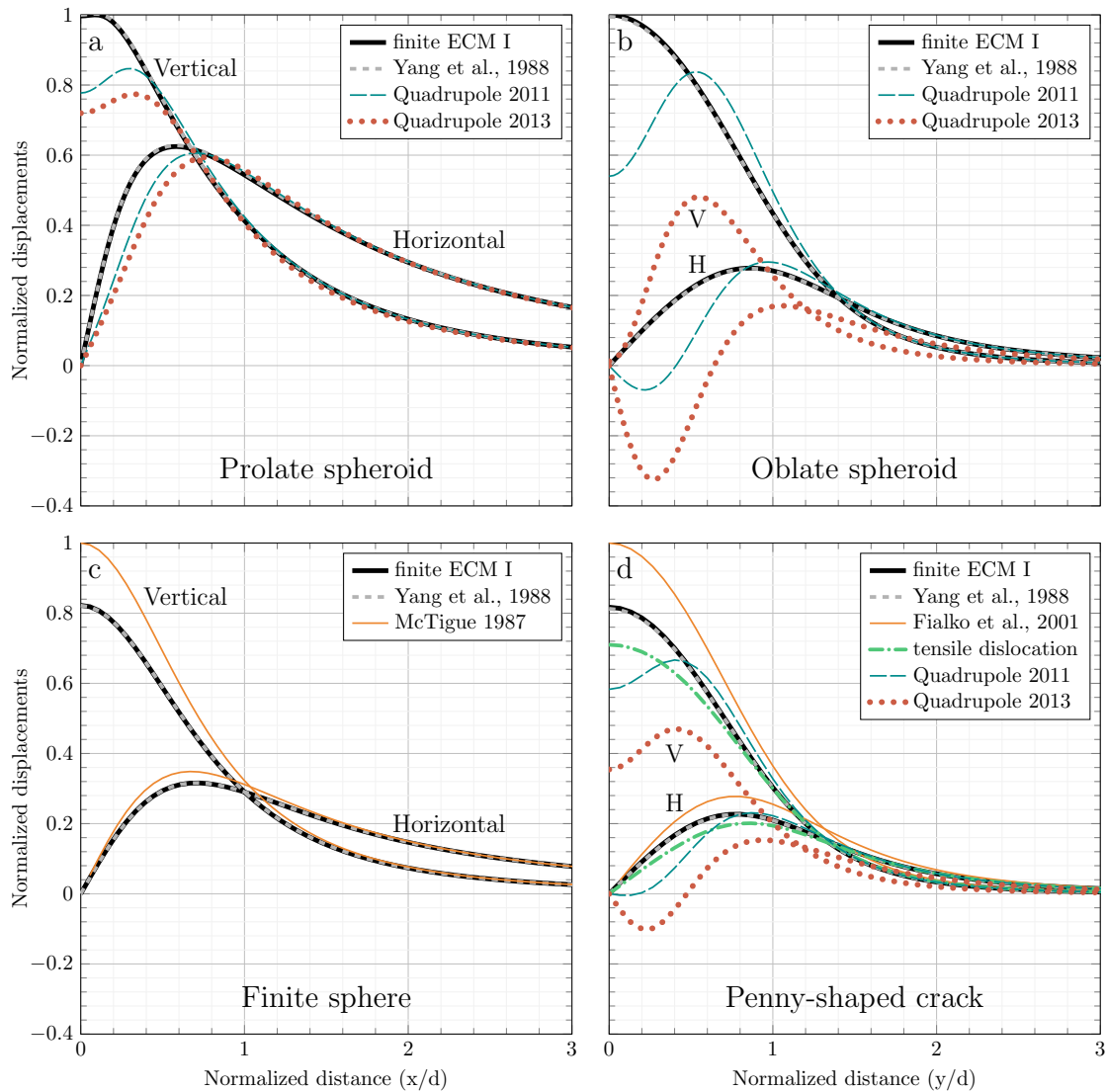


Figure 2. Comparison of the finite ECM with selected analytical solutions. “Quadropole 2011” and “Quadropole 2013” refer to the Amoruso & Crescentini (2011) and Amoruso & Crescentini (2013) models. For all displacements, normalization method I has been used. The horizontal and vertical displacements are indicated in a) and c). The curves below “H” and those above “V” in b) and d) represent the horizontal and vertical displacements, respectively. In all cases $\omega_x = \omega_y = \omega_z = 0^\circ$. a) Comparison with a prolate spheroid. Source parameters are $a_x/a_z = 1/3$, $a_x = a_y$ and $a_z/d_C = 5/6$, and $N = 3297$. b) Comparison with an oblate spheroid. Source parameters are $a_x/a_z = 18$, $a_x = a_y$ and $a_z/d_C = 1/18$, and $N = 1439$. c) Comparison with the finite spherical source. Source parameters are $a_x = a_y = a_z = R$ and $R/d_C = 0.556$, and $N = 385$. d) Comparison with the penny-shaped crack and a square tensile dislocation (Okada 1985). Source parameters are $a_z/a_x = 10^{-6}$, $a_x = a_y$ and $a_x/d_C = 0.867$, and $N = 933$. The square dislocation has the same potency as the finite ECM and its edge length is $(\pi a_x^2)^{1/2}$.

12 *Mehdi Nikkhoo, Eleonora Rivalta*

Table 1. Systematic comparison of the Yang et al. (1988) solution (prolate and oblate spheroids) with the finite ECM for varying c_r^* , and convergence test of the finite ECM for triaxial ellipsoids. $\overline{t_C}$ is the mean computation time, $\max \epsilon_x$ and $\max \epsilon_z$ are the maximum relative errors for the u_x and u_z components of the surface displacements, respectively, and $\alpha(\epsilon_x < 0.01)$ and $\alpha(\epsilon_z < 0.01)$ are the ~~percentages of cases with relative errors below 1 per cent~~ percent of models with errors smaller than 0.01. The comparison involves 3800 prolate spheroids with parameters $x_0 = y_0 = 0$ m, $d_C \in [100, 1000]$ m, $a_z = 1000$ m, $a_x = a_y \in [50, 950]$ m, $\omega_x = \omega_z = 0^\circ$, $\omega_y \in [0^\circ, 90^\circ]$. ~~For $c_r^* = 10$, we have $N_{\min} = 20$, $N_{\max} = 2884$, whereas for $c_r^* = 20$ we have $N_{\min} = 163$ and $N_{\max} = 15035$.~~ The comparison also involves 3716 oblate spheroids, with parameters $a_x = a_y = 1000$ m and $a_z \in [50, 950]$ m; all the other parameters are the same as those for the prolate sources. ~~For oblate cavities, $c_r^* = 10$ leads to $N_{\min} = 20$ and $N_{\max} = 1413$, and $c_r^* = 20$ results in $N_{\min} = 163$ and $N_{\max} = 11410$.~~ The convergence test involves 5868 triaxial ellipsoids, with parameters $x_0 = y_0 = 0$ m, $d_C \in [1000, 2000]$ m, $a_x = 1000$ m, $a_y \in [50, 950]$ m, $a_z \in [50, 950]$ m and $\omega_y \in [0^\circ, 90^\circ]$. For these ellipsoids the finite ECM solution with $c_r^* = 12$ is compared to the solution with $c_r^* = 20$. In all cases, the surface observation grid consists of 496 points with a spacing of 200 m within $x \in [-3000, 3000]$ m and $y \in [0, 3000]$ m. For all sources $d_T \geq 200$ m.

c_r^*	N_{\min}	N_{\max}	$\overline{t_C}$	$\max \epsilon_x$	$\max \epsilon_z$	$\alpha(\epsilon_x < 0.01)$	$\alpha(\epsilon_z < 0.01)$
			[s]	[%]	[%]	[%]	[%]
Prolate spheroids							
10	20	2884	0.097	0.012	0.021	98.9	90.0
12	29	4010	0.17	0.0088	0.014	100	98.5
14	57	4018	0.27	0.0076	0.013	100	99.4
20	163	15035	0.79	0.0045	0.0073	100	100
Oblate spheroids							
10	20	1413	0.10	0.034	0.049	85.0	53.0
12	29	2456	0.17	0.027	0.035	87.7	80.0
14	57	3918	0.27	0.021	0.028	99.5	91.3
20	163	11410	0.80	0.009	0.013	100	99.8
Triaxial ellipsoids							
12	111	2985	0.40	0.015	0.028	99.7	95.7

282 show that the Amoruso & Crescentini (2011) and Amoruso & Crescentini (2013) models perform well
 283 for a range of rather shallow, vertically-elongated sources.

284 The second comparison (Fig. 2b) involves the same analytical solutions, but for an oblate spheroid
 285 (Yang et al. 1988; Cervelli 2013) with $a_x/a_z = 18$ and $a_x/d_C = 1$. Again, the finite ECM and the Yang

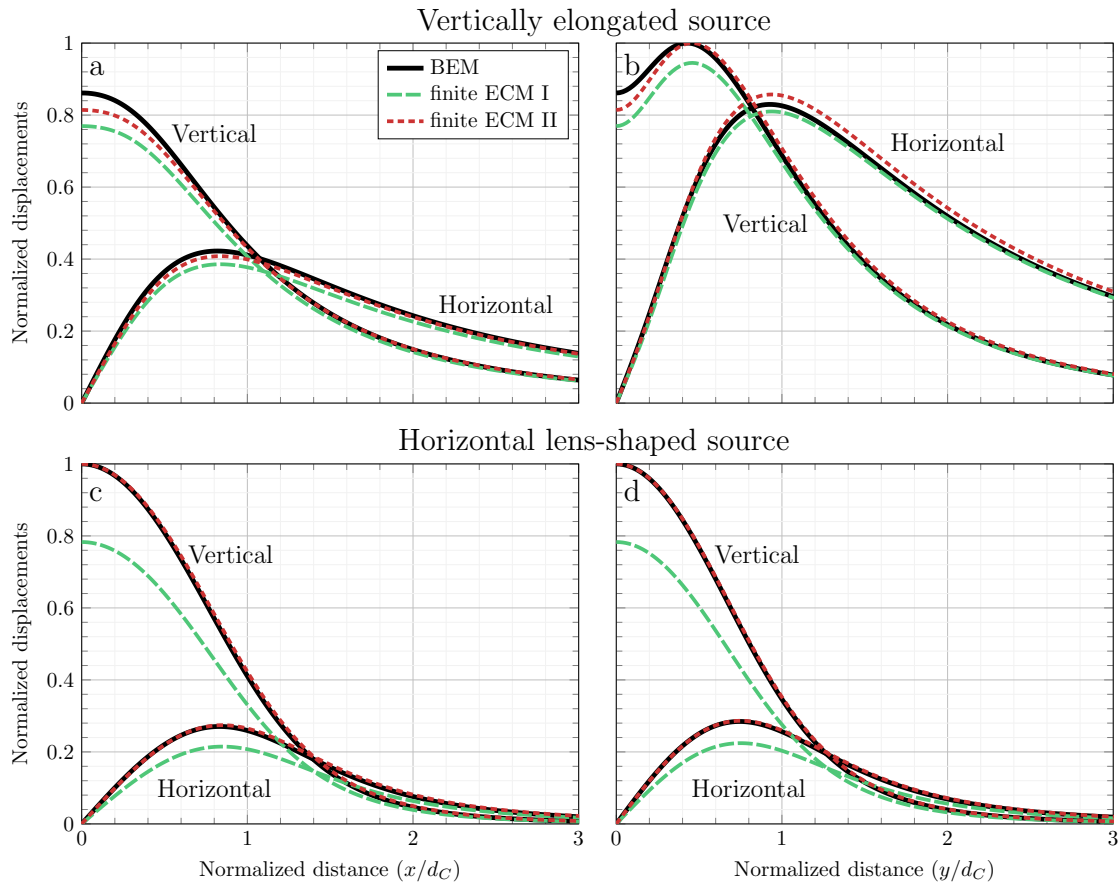


Figure 3. Comparison with selected numerical solutions for triaxial sources. The black solid lines are BEM solutions. The gray and green solid lines are the finite ECM displacements, normalized through methods I and II, respectively (see text). a) Vertically elongated source with $a_x/a_z = 1/2$, $a_y/a_z = 1/3$, $a_z/d_C = 1/2$ and $\omega_x = \omega_y = \omega_z = 0^\circ$. Displacements are shown for the xz plane. b) Same as a), but for the yz plane. c) Lens-shaped source with $a_x/a_z = 15$, $a_y/a_z = 12$, $a_z/d_C = 15$ and $\omega_x = \omega_y = \omega_z = 0^\circ$. Displacements are shown for the xz plane. d) Same as c), but for the yz plane. The finite ECM is shown for $c_1^* = 14$ which leads to $N = 260$ and $N = 1439$ for the vertically elongated source (a and b) and the horizontal lens-shaped source (c and d), respectively.

et al. (1988) solutions are almost identical; however, the Amoruso & Crescentini (2011) and Amoruso & Crescentini (2013) models break down with large errors, especially for the horizontal displacements. Interestingly, the Amoruso & Crescentini (2011) solution, which is a finite difference approximation of the Amoruso & Crescentini (2013) quadrupole solution, works better than the Amoruso & Crescentini (2013) model. We will expand on the underlying reason later.

The next comparison involves the McTigue (1987) and Yang et al. (1988) solutions in the case of a sphere (Fig. 2c). The mismatch between the McTigue (1987) and the Yang et al. (1988) and finite ECM solutions is because both the latter solutions involve the Davis approximation, while the

1
2
3
4 14 *Mehdi Nikkhoo, Eleonora Rivalta*

5
6 294 McTigue (1987) solution contains higher-order terms correcting for the resulting misrepresentation
7 295 of the boundary conditions on the cavity walls. For spherical cavities (except for the McTigue 1987,
8 296 solution) the surface displacements from the finite-source solutions (Yang et al. 1988, and the finite
9 297 ECM) are in theory expected to be identical to their equivalent point-source solutions (Mogi 1958;
10 298 Davis 1986, and the point CDM). The Amoruso & Crescentini (2011) and Amoruso & Crescentini
11 299 (2013) models are also comparable to those models. Thus, for the sake of clarity, we only show the
12 300 McTigue (1987), Yang et al. (1988) and the finite ECM displacements in Fig. 2c.

13
14
15
16
17 301 As the last analytical comparison, we consider a uniformly pressurized penny-shaped crack (Sun
18 302 1969; Fialko et al. 2001), the Yang et al. (1988) solution, a horizontal tensile square dislocation (Davis
19 303 1983; Okada 1985), and again, the Amoruso & Crescentini (2011) and Amoruso & Crescentini (2013)
20 304 models. For this special case, the finite ECM has only one layer of point sources with varying po-
21 305 tencies. Again, there is an excellent agreement between the finite ECM and the Yang et al. (1988)
22 306 solution; also the Sun (1969) solution (not shown in Fig. 2d) perfectly agrees with these solutions.
23 307 The difference with the Fialko et al. (2001) solution is due to the fact that the boundary conditions on
24 308 the source walls are more accurately implemented in the Fialko et al. (2001) solution. However, com-
25 309 pared to the square dislocation, the finite ECM and the Yang et al. (1988) solutions provide a better
26 310 approximation to the Fialko et al. (2001) solution. This is because the opening of the square disloca-
27 311 tion is uniform while the opening of the cracks represented by the Yang et al. (1988) solution and finite
28 312 ECM have an elliptic form. This feature is implemented through step “7” of the adaptive algorithm.
29 313 Also in this case, the Amoruso & Crescentini (2011) solution performs better than the Amoruso &
30 314 Crescentini (2013) model. Both models, however, perform well only in the far field.

31
32
33
34
35
36
37
38
39
40 315 Finally, we compare the finite ECM with numerical solutions for 114 uniformly-pressurized triax-
41 316 ial ellipsoids involving a wide range of parameters (see [Table S1 in Supplementary Information](#)). We
42 317 calculate the surface displacements and volume changes associated with the triaxial cavities by using
43 318 the Nikkhoo & Walter (2015) half-space solution for Triangular Dislocations (TDs; see also Yoffe
44 319 1960; Comninou & Dundurs 1975) in a numerical scheme based on the Boundary Element Method
45 320 (BEM; see Crouch 1976; Crouch & Starfield 1983; Kuriyama & Mizuta 1993). We illustrate the sur-
46 321 face displacements associated with two representative cases (see Fig. 3). For the vertically elongated
47 322 cavity, we find that, except for the vertical displacements right above the ellipsoid, the finite ECM
48 323 and BEM solutions are nearly identical (Fig. 3a,b). The agreement is best along the y -axis, which is
49 324 parallel to the semi-minor axis. For the second source, which is sill-like, the agreement is not as good
50 325 (Fig. 3c,d). However, the functional shape of the solutions is very similar: indeed, a substantially better
51 326 agreement is achieved if the displacements are normalized by method II (Fig. 3c,d). This implies that
52 327 applying the finite ECM and Yang et al. (1988) solution (the Cervelli 2013, code) to source inversions
53
54
55
56
57
58
59
60

involving sill-like sources may lead to fairly good constraints on the source shape, but the volume change and depth of the source may be biased considerably.

We further perform a systematic comparison between the finite ECM and BEM surface displacements and volume changes for the 114 triaxial ellipsoids (see [Table S1 in Supplementary Information](#)). For these ellipsoids we calculate the volume change, δV , the horizontal and vertical surface displacements along the x axis, (u_x^h, u_x^v) , and those along the y axis, (u_y^h, u_y^v) . The relative volume change misfit is calculated as

$$\epsilon_{\delta V} = \frac{|\delta V(\text{fECM}) - \delta V(\text{BEM})|}{\delta V(\text{BEM})}, \quad (9)$$

where “fECM” and “BEM” refer to the finite ECM and BEM calculations, respectively. Also, we use

$$\epsilon_x^h = \frac{\int_0^{3d_C} |u_x^h(\text{fECM}) - u_x^h(\text{BEM})| dx}{\int_0^{3d_C} |u_x^h(\text{BEM})| dx}, \quad (10)$$

as a measure of misfit between $u_x^h(\text{fECM})$ and $u_x^h(\text{BEM})$. Similarly, we calculate ϵ_x^v , ϵ_y^h and ϵ_y^v as misfits between the finite ECM and BEM displacement components u_x^v , u_y^h and u_y^v , respectively. We define

$$\begin{aligned} \epsilon^h &= \frac{\epsilon_x^h + \epsilon_y^h}{2}, \\ \epsilon^v &= \frac{\epsilon_x^v + \epsilon_y^v}{2}, \end{aligned} \quad (11)$$

as the mean horizontal and mean vertical misfits. We calculate such misfit for displacements normalized by both method I and method II as ϵ_I^h , ϵ_I^v , ϵ_{II}^h and ϵ_{II}^v . To determine the range of applicability of the finite ECM we evaluate the mean horizontal and vertical misfits as a function of d_C/a_C , d_T/a_C , d_T/ρ_T^{\max} and d_T/ρ_T^{\min} (see [Table S1 in Supplementary Information](#)). The results show that

1. d_T/ρ_T^{\max} and d_T/ρ_T^{\min} are only useful for vertical prolate sources as they miscalculate oblate and triaxial sources and also, rotated prolate sources.
2. the misfits ϵ_I^h and ϵ_I^v are below 10% and 15% for $d_C/a_C \gtrsim 1.75$ and $d_C/a_C \gtrsim 1.25$, respectively.
3. the misfits ϵ_{II}^h and ϵ_{II}^v are below 7% and 15% for $d_T/a_C \gtrsim 0.7$ and $d_T/a_C \gtrsim 0.5$, respectively.
4. $\epsilon_{\delta V}$ is smaller than 10% and 5% for $d_C/a_C \gtrsim 1.75$ and $d_C/a_C \gtrsim 2.5$, respectively. The largest $\epsilon_{\delta V}$ values correspond to shallow oblate ellipsoids. For very shallow oblate cavities $\epsilon_{\delta V}$ may become extremely large, occasionally even exceeding 100% (see “D0”, “P0”, “P1”, “Q0” and “Q1” cases in [Table S1 in Supplementary Information](#)).

Note that the criteria based on d_C/a_C and d_T/a_C are in agreement with the Amoruso et al. (2007) criterion, $d_C/a_C \gtrsim 0.8$, for penny-shaped cracks.

The d_T/ρ_T^{\max} for the cavities in Fig. 2a-d are 1.8, 0.053, 0.8 and 0, respectively; the d_C/a_C are 1.2, 1, 1.8 and 1, respectively; and the d_T/a_C are 0.2, 0.94, 0.8 and 1, respectively. Thus, all these cavities

1
2
3
4 16 *Mehdi Nikkhoo, Eleonora Rivalta*

5
6 360 satisfy at least one of the criteria listed above: the cavity in Fig. 2a satisfies $d_T/\rho_T^{\max} \gtrsim 1$, the cavity
7 361 in Fig. 2b satisfies the criteria based on d_C/a_C and d_T/a_C , the cavity in Fig. 2c satisfies the criteria
8 362 based on d_T/ρ_T^{\max} , d_C/a_C and d_T/a_C , and the cavity in Fig. 2d satisfies the criteria based on d_C/a_C
9 363 and d_T/a_C .

10
11
12 364 The comparisons above show that the finite ECM is a reliable model for shallow triaxial sources,
13 365 beyond what previously published solutions offer.

14 15 16 17 18 366 **4 DISCUSSION**

19 20 367 **4.1 The approximations involved in the finite ECM and the other solutions**

21
22 368 We developed the finite ECM in the form of distributed point CDMs having depth-dependent strengths
23 369 but the same aspect ratio determined through the Eshelby (1957) shape functions (eq. 1). Unless the
24 370 cavity shape is spherical, spheroidal or crack-like, these functions involve elliptic integrals, which can
25 371 be calculated only numerically (see Carlson 1995). All other components of the finite ECM—all steps
26 372 of the adaptive algorithm controlling the configuration of the solution—are analytical.

27
28
29 373 Distributed point sources have been proposed in earlier works as a straightforward approach to
30 374 simulate the near field deformations caused by shallow pressurized cavities with non-negligible char-
31 375 acteristic dimension in comparison with the cavity depth (see Davis 1986; Wang et al. 2018). Amoruso
32 376 et al. (2007) used a uniform distribution of point sources (Wang et al. 2006, semi-analytical solution) to
33 377 simulate the surface displacements associated with a horizontal penny-shaped crack in a layered half-
34 378 space, and applied it to the 2004–2006 uplift period at Campi Flegrei caldera. Also, Amoruso et al.
35 379 (2008) used a similar approach for the joint inversion of surface displacements and gravity changes
36 380 recorded during the 1982–1984 unrest period at Campi Flegrei. The finite ECM can facilitate similar
37 381 inversions for generic ellipsoidal geometries.

38
39
40 382 The calibration and systematic comparisons between the finite ECM and the Yang et al. (1988)
41 383 solution for a few thousand prolate and oblate cavities show that for $c_r^* \geq 14$ the mismatch between
42 384 the surface displacements from the two models are $\lesssim 1\%$ (Table 1). For most rapid source inversions,
43 385 $c_r^* = 10$ may be optimal, as it provides acceptable accuracy for reasonably short computation times.
44 386 If it is clear from preliminary inversions (e.g. using the point CDM) that the source is prolate, smaller
45 387 values for c_r^* may be sufficient. In any case, starting an inversion with the point CDM, before switching
46 388 to the finite ECM first with $c_r^* = 10$ and then higher c_r^* s for more limited parameter space may be a
47 389 good procedure to follow.

48
49
50 390 Compared with the finite ECM, the Amoruso & Crescentini (2011) and Amoruso & Crescentini
51 391 (2013) models require shorter computation times and thus, could potentially be useful for rapid source
52
53
54
55
56
57
58
59
60

1
2
3
4
5
6 392 inversions. However, this demands a rigorous assessment of the range of applicability of these models.
7 393 This is especially necessary regarding shallow oblate sources, for which the displacement patterns
8
9 394 from the Amoruso & Crescentini (2011) and Amoruso & Crescentini (2013) models may perform
10 395 worse than point source solutions such as the Davis (1986) or the point CDM (Fig. 2b,d).

11
12 396 The fluctuations of the Amoruso & Crescentini (2011) and Amoruso & Crescentini (2013) models
13
14 397 for shallow oblate sources, together with the interesting observation that the 7-point-source solution,
15 398 at least in those cases from Fig 2, performs better than the Amoruso & Crescentini (2013) model call
16
17 399 for an explanation. To understand the reason for this, it is important to note that, although both the
18
19 400 Amoruso & Crescentini (2011) and Amoruso & Crescentini (2013) models are based on the same
20 401 “quadrupole approximation”, there are inherent differences between the two models. The Amoruso &
21 402 Crescentini (2013) model is in fact a higher-order point-source model—it represents a special case of
22
23 403 a rank-4 moment tensor. On the other hand, the Amoruso & Crescentini (2011) model is formed as
24
25 404 the superposition of 7 rank-2 moment tensors of both positive and negative sign, distributed within the
26
27 405 cavity. This distributed configuration gives the source some “finiteness”, which might be what makes
28 406 the 7-point-source model perform better, at least in the examined cases, than a rank-4 moment tensor.
29
30 407 In the far field, these models reduce to a rank-2 moment tensor, but for oblate sources in the near field
31 408 this fails to happen.

32
33 409 Among analytical volcano deformation sources, the McTigue (1987) and Fialko et al. (2001) so-
34
35 410 lutions fulfil very accurately (although still not exactly) the uniform-pressure boundary conditions on
36
37 411 the source walls. All the other available analytical source models, including Sun (1969); Yang et al.
38 412 (1988); Amoruso & Crescentini (2011, 2013) and the finite ECM, make use of the Davis approxima-
39 413 tion. Therefore, inferring the parameters of uniformly pressurized magma bodies by using the latter
40 414 group of source models may come with a substantial bias if the source is very shallow. Examples
41 415 of this can be seen in Fig. 3a-d, where a perfect fit is achieved for oblate sources, but with a biased
42
43 416 volume change. As also shown by Amoruso & Crescentini (2011), such a bias is likely to emerge on
44
45 417 depth and source aspect ratio, beside volume change. Similarly, biases on the spatial orientation of the
46
47 418 source could be expected. The extent of these biases as a function of source depth and shape has not
48
49 419 been thoroughly investigated yet and should be addressed by future studies.

50
51 420 Our results concerning the normalization method I and method II, which we used in section 3,
52
53 421 have direct implications for forward and inverse modelling using the finite ECM or any other source
54
55 422 model involving the Davis approximation. Suppose that the surface displacements associated with a
56
57 423 given pressurized cavity are calculated by using two different source models: an accurate model and
58
59 424 an approximate model. Applying the normalization method I preserves the relative misfit between the
60 425 displacements from the two models—this misfit reflects the actual accuracy (or error) associated with

1
2
3
4 18 *Mehdi Nikkhoo, Eleonora Rivalta*

5
6 426 the approximate model for a given set of parameters. Evaluating this misfit is important when using
7 427 the approximate model for forward modelling purposes (e.g. analyzing the synthetic displacements
8 428 expected for a certain cavity). On the other hand, applying normalization method II scales the dis-
9 429 placements such that the maximum vertical displacements from the two models become equal to 1.
10
11 430 This leads to overall smaller misfits for the normalized displacements. The implication is that the ap-
12 431 proximate model may lead to an acceptable, or even an excellent, fit when used for inverse modelling
13 432 of actual deformation data measured in the field. A significant difference between the misfits from
14 433 normalization method I and those from normalization method II imply that, in an inversion using the
15 434 approximate source, the source strength (volume change), and possibly other source parameters, may
16
17
18
19
20 435 be misestimated.
21
22

23 436 **4.2 The added value of triaxial finite-source solutions**

24
25 437 The deformation signals measured at the Earth's surface can be used to infer some large-scale features
26 438 of pressurized magma chambers. These large-scale features are in fact the deformation source param-
27 439 eters, which can be constrained through deformation modelling. For deep sources, these parameters
28
29 440 are limited to the location, spatial orientation and strength; in this case point-source and finite-source
30 441 models yield the same results. For shallow sources, in addition to the location, spatial orientation and
31 442 strength, it is possible to constrain the source dimensions, provided that displacement data in the near-
32 443 field are available. Finite triaxial sources help better constrain the aspect ratio and size, and thus, the
33 444 volume of pressurized magma bodies. This would be of great benefit, as the overall volume of magma
34
35 445 reservoirs is a poorly constrained quantity in volcanology. In this case, point-source solutions can-
36 446 not be used because they cannot represent the displacements in the near field. Therefore, to infer the
37 447 parameters of shallow magma chambers correctly, finite-source models need to be used.
38
39

40
41 448 It is difficult to estimate how often a triaxial finite source can be applied. So far, triaxial point
42 449 sources were applied to study the geometry of magma storage at Kilauea volcano (Davis 1986) and
43 450 Long Valley caldera (Langbein et al. 1995), to constrain a draining magma reservoir at Calbuco volcano
44 451 (Nikkhoo et al. 2017), offshore Mayotte (Cesca et al. 2020) and Erta Ale volcano (Xu et al. 2020),
45 452 and to track magma ascent at Piton de la Fournaise (Beauducel et al. 2020b). A finite triaxial source
46 453 may help better explore some of these cases, or constrain other unexplored cases involving shallow
47 454 sources.
48
49

50
51 455 In standard inversion procedures, different analytical solutions are tested one by one searching for
52 456 an optimal match with observations. Nikkhoo et al. (2017), Beauducel et al. (2020b) and Peltier et al.
53 457 (2020) showed the benefit of avoiding such one-by-one matching and relying on the ability of the point
54 458 CDM to span the entire model space with just one model. By feeding the data into such an automatic
55
56
57
58
59
60

1
2
3
4
5
6 459 procedure, it is possible to reveal the underlying cause of the deformation, be it the (de)pressurization
7 460 of an equi-dimensional body such as a reservoir (Cesca et al. 2020; Xu et al. 2020), or the propagation
8 461 of a dike (Sigmundsson et al. 2015; Xu et al. 2016; Dumont et al. 2018; Beauducel et al. 2020b; Peltier
9 462 et al. 2020; Davis et al. 2021). The finite ECM extends this capability to deformation sources in the
10 463 near field.
11
12
13
14

15 464 **4.3 The volume change and the compressibility associated with the finite ECM**

16
17 465 In order to fully characterize a volcano deformation source, it is critical to provide the practical means
18 466 to calculate the volume change upon pressurization. The volume change is a measure of the source
19 467 strength and can be used to estimate other important quantities such as the chamber compressibility,
20 468 defined as the relative volume change for a unit pressurization. The chamber compressibility, together
21 469 with the magma compressibility, is critical to estimate the real intrusion volume.
22
23
24

25 470 The volume change associated with ellipsoidal sources in a full space can be calculated from the
26 471 Eshelby (1957) solution (see Amoruso & Crescentini 2009, 2013). This “full-space” volume change is
27 472 also used as an approximation for the half-space models. This is because the exact volume change in
28 473 half-space source models cannot be calculated analytically. One caveat is that the volume change for
29 474 shallow sources in a half-space may be substantially different from the full-space volume change—
30 475 accurate half-space volume change calculations require numerical methods (see Amoruso & Cres-
31 476 centini 2009; Anderson & Segall 2011). Since volume change and chamber compressibility may be
32 477 important magma chamber properties both for inversions and for forward modelling of eruptive vol-
33 478 umes (Mastin et al. 2008; Anderson & Segall 2011; Wasser et al. 2021), we include codes based on the
34 479 Eshelby (1957) approach for the accurate calculation of the full-space volume change and chamber
35 480 compressibility (see Segall et al. 2001; Rivalta & Segall 2008; Segall 2010).
36
37
38
39
40
41
42
43

44 481 **4.4 Implications for modelling deformation-induced gravity changes**

45
46 482 Okubo (1991) developed an analytical solution for surface gravity changes caused by point disloca-
47 483 tions. Based on Okubo (1991)’s work, Nikkhoo & Rivalta (2022) developed an analytical solution
48 484 for deformation-induced gravity changes associated with the point CDM. We use the Nikkhoo & Ri-
49 485 valta (2022) point-source solution for gravity changes within the adaptive algorithm in section 2.1 to
50 486 develop the gravity change solution associated with the finite ECM.
51
52
53

54 487 A major contribution to the surface gravity changes caused by any deformation source is due to the
55 488 source volume change (e.g., Okubo 1991; Nikkhoo & Rivalta 2022). Considering that the estimated
56 489 volume change for the finite ECM may be subject to large biases (see section 3), caution is advised
57 490 while applying the finite ECM to joint inversions of surface deformations and gravity changes.
58
59
60

20 *Mehdi Nikkhoo, Eleonora Rivalta*

5 CONCLUSIONS

1. We developed a computationally-efficient solution for the surface deformation field caused by a finite triaxial ellipsoidal source in the form of a non-uniform (depth-dependent) distribution of point CDMs. The finite ECM is especially suitable for inversions of surface deformation data.
2. The finite ECM includes an adaptive algorithm that determines the optimal spacing and location of the point CDMs as a function of the depth, shape, and spatial orientation of the cavity, and a grid-spacing parameter c_T^* .
3. We showed that the Yang et al. (1988) solution can be used to benchmark the finite ECM and calibrate c_T^* , or alternatively N_{\max} , to achieve any desired accuracy while maintaining computation time minimal. We further validated the finite ECM through comparisons with other analytical and numerical solutions.
4. Through comparisons with numerical solutions we found new empirical criteria for the accuracy of the finite ECM calculations. As rules of thumb, a finite ECM with $d_C/a_C \gtrsim 2$ yields excellent results—this criterion is especially useful for forward modelling of the surface displacements; a finite ECM with $d_T/a_C \gtrsim 1$ performs very well in source inversions, with the caveat that some parameters (especially volume change and depth) may be biased. Our results show that the Yang et al. (1988) criterion ($d_T \gtrsim \rho_T$) is only appropriate for vertical prolate spheroids and cannot be extended to triaxial ellipsoids.
5. We provide MATLAB codes for the finite ECM (surface displacements and deformation-induced gravity changes) and additional codes to calculate the volume change and chamber compressibility of ellipsoidal sources. The codes do not contain any MATLAB-specific function and it is straightforward to convert them to any other programming language.

ACKNOWLEDGMENTS

The authors thank Yosuke Aoki, an anonymous reviewer and the editor for their constructive comments. The authors appreciate the hospitality and financial support of the ICTP solid earth geophysics group. This research was funded by the EU Horizon 2020 programme NEWTON-g project, under the FET-OPEN-2016/2017 call (Grant Agreement No 801221) and by the German Research Foundation (DFG), Grant 634756, RI 2782/2.

DATA AVAILABILITY

The MATLAB codes associated with this research are available to download at

521 <https://volcanodeformation.com/onewebmedia/fECM.zip>. Further details about the model and
522 other related codes can be found under <https://www.volcanodeformation.com/>.

523 APPENDIX A: ANALYTICAL SOLUTIONS FOR THE SHALLOWEST AND DEEPEST 524 POINTS ON THE SURFACE OF A GENERIC ELLIPSOID

525 The standard ellipsoid E_S centered at the origin of a Cartesian xyz coordinate system has the form

$$526 \frac{x^2}{a_x^2} + \frac{y^2}{a_y^2} + \frac{z^2}{a_z^2} = 1, \quad (\text{A.1})$$

527 where the semi-axes a_x , a_y and a_z are aligned with the x , y and z coordinate axes, respectively. If
528 (θ, λ) denote the spherical coordinates, of an arbitrary point P on the surface of E_S , we have

$$\begin{aligned} 529 x &= a_x \sin \theta \cos \lambda, \\ 530 y &= a_y \sin \theta \sin \lambda, \\ 531 z &= a_z \cos \theta, \end{aligned} \quad (\text{A.2})$$

532 where $\theta \in [0, \pi]$ and $\lambda \in [0, 2\pi)$. The matrices

$$\begin{aligned} 534 R_x(\omega_x) &= \begin{pmatrix} 1 & 0 & 0 \\ 0 & \cos \omega_x & \sin \omega_x \\ 0 & -\sin \omega_x & \cos \omega_x \end{pmatrix} \\ 535 \\ 536 R_y(\omega_y) &= \begin{pmatrix} \cos \omega_y & 0 & -\sin \omega_y \\ 0 & 1 & 0 \\ \sin \omega_y & 0 & \cos \omega_y \end{pmatrix}, \\ 537 \\ 538 R_z(\omega_z) &= \begin{pmatrix} \cos \omega_z & \sin \omega_z & 0 \\ -\sin \omega_z & \cos \omega_z & 0 \\ 0 & 0 & 1 \end{pmatrix}, \end{aligned} \quad (\text{A.3})$$

539 represent general rotations about the x , y and z axes, respectively. Any arbitrary rotation in xyz can
540 be represented in the form of

$$541 R = R_x(\omega_x) R_y(\omega_y) R_z(\omega_z) = \begin{pmatrix} r_{11} & r_{12} & r_{13} \\ r_{21} & r_{22} & r_{23} \\ r_{31} & r_{32} & r_{33} \end{pmatrix}, \quad (\text{A.4})$$

22 *Mehdi Nikkhoo, Eleonora Rivalta*

542 with a unique set of angles $(\omega_x, \omega_y, \omega_z)$. After applying such a rotation, the new coordinates of P are

$$543 \begin{pmatrix} x' \\ y' \\ z' \end{pmatrix} = \begin{pmatrix} r_{11} & r_{12} & r_{13} \\ r_{21} & r_{22} & r_{23} \\ r_{31} & r_{32} & r_{33} \end{pmatrix} \begin{pmatrix} x \\ y \\ z \end{pmatrix}. \quad (\text{A.5})$$

544 Combining equations A.5 and A.2 yields

$$545 z' = r_{31}a_x \sin \theta \cos \lambda + r_{32}a_y \sin \theta \sin \lambda + r_{33}a_z \cos \theta. \quad (\text{A.6})$$

546 The spherical coordinates of the two points with the minimum and maximum z values on the ellipsoid
547 are the solutions of the equation

$$548 \frac{\partial z'}{\partial \lambda} = 0, \quad \frac{\partial z'}{\partial \theta} = 0, \quad (\text{A.7})$$

549 that can be written in explicit form as

$$550 \lambda = \text{atan} \left(\frac{r_{32}a_y}{r_{31}a_x} \right), \quad \theta = \text{atan} \left(\frac{\sqrt{r_{31}^2 a_x^2 + r_{32}^2 a_y^2}}{r_{33}a_z} \right). \quad (\text{A.8})$$

551 **APPENDIX B: AN ANALYTICAL EXPRESSION FOR THE VOLUME OF A PARTITION** 552 **OF AN ELLIPSOID BOUNDED BY TWO HORIZONTAL PLANES**

553 Let C_P denote the ellipsoidal cap formed by the intersection of the standard ellipsoid, E_S (equation
554 A.1) and an arbitrary plane, $S : Ax + By + Cz = D$, where the vector (A, B, C) is normal to the
555 plane and points towards C_P . The volume of C_P is

$$556 V_P(S) = \iiint_{C_P} dx dy dz. \quad (\text{B.1})$$

557 In a new Cartesian XYZ coordinate system, where $x = a_x X$, $y = a_y Y$ and $z = a_z Z$ the ellipsoid
558 is mapped onto the unit sphere, $X^2 + Y^2 + Z^2 = 1$, and the plane is mapped onto the new plane
559 $S' : Aa_x X + Ba_y Y + Ca_z Z = D$. Also, equation B.1 can be rewritten as

$$560 V_P(S) = V_P(S') = a_x a_y a_z \iiint_{C'_P} dX dY dZ, \quad (\text{B.2})$$

561 where

$$562 \iiint_{C'_P} dX dY dZ = \frac{1}{3} \pi (1 - d_n)^2 (2 + d_n), \quad (\text{B.3})$$

563 is the volume of the spherical cap, C'_P , that is bounded by the unit sphere and the new plane (see Kern
564 & Bland 1938, p. 37 and Harris & Stöcker 1998, p. 107) and $d_n = D / (A^2 a_x^2 + B^2 a_y^2 + C^2 a_z^2)^{1/2}$ is
565 the shortest distance from the origin of XYZ to the new plane. Substituting equation B.3 in equation

566 B.2 yields:

$$567 \quad V_P(S) = \frac{1}{3}\pi a_x a_y a_z (1 - d_n)^2 (2 + d_n). \quad (\text{B.4})$$

568 Thus, the volume of the region inside E_S and bounded by two parallel planes $S_1 : Ax + By + Cz = D_1$
569 and $S_2 : Ax + By + Cz = D_2$ can be calculated as

$$570 \quad V_{D_1 D_2} = |V_P(S_2) - V_P(S_1)|. \quad (\text{B.5})$$

571 For an arbitrary ellipsoid subjected to the rotations $R_x(\omega_x)R_y(\omega_y)R_z(\omega_z)$ and centered at $(x_0, y_0, -d)$,
572 the volume of the region inside the ellipsoid and bounded by two horizontal planes $z = z_1$ and
573 $z = z_2$ can be calculated from equation B.5 after applying the translation $(-x_0, -y_0, d)$ and rotations
574 $R_z(-\omega_z)R_y(-\omega_y)R_x(-\omega_x)$ to the ellipsoid and both planes.

575 APPENDIX C: INTERSECTION OF A PLANE AND AN ARBITRARY ELLIPSOID

576 In order to determine the intersection ellipse associated with a horizontal plane, $S_H : z = z_j$, and an
577 arbitrary ellipsoid E_R subjected to the rotations $R_x(\omega_x)R_y(\omega_y)R_z(\omega_z)$ and centered at $(x_0, y_0, -d)$,
578 we first apply the translation $(-x_0, -y_0, d)$ and rotations $R_z(-\omega_z)R_y(-\omega_y)R_x(-\omega_x)$ to both E_R and
579 S_H . These transformations lead to a standard ellipsoid E_S (equation A.1), and a plane of the form
580 $S : Ax + By + Cz = D$. The intersection ellipse formed by E_S and S can be determined through the
581 Klein (2012) formulas. Applying the rotations $R_x(\omega_x)R_y(\omega_y)R_z(\omega_z)$ and the translation $(x_0, y_0, -d)$
582 to the ellipse from the previous step yields the solution.

583 APPENDIX D: PRINCIPAL CURVATURES AT ANY POINT ON THE SURFACE OF AN 584 ELLIPSOID

585 The principal curvatures, κ_{\max} and κ_{\min} , at any point $P(\theta, \lambda)$ on the surface of the standard ellipsoid
586 (equation A.1) are the solutions of the following equation:

$$587 \quad (EG - F^2)\kappa^2 - (EN + GL - 2FM)\kappa + (LN - M^2) = 0, \quad (\text{D.1})$$

588 where E , F and G are the first fundamental coefficients and L , M and N are the second fundamental
589 coefficients of the ellipsoid (see Lipschutz 1969, p. 183). A simplified form of equation D.1 can be
590 written as

$$591 \quad A\kappa^2 + B\kappa + C = 0, \quad (\text{D.2})$$

24 Mehdi Nikkhoo, Eleonora Rivalta

where

$$\begin{aligned}
 A &= (a_x^2 \cos^2 \theta \cos^2 \lambda + a_y^2 \cos^2 \theta \sin^2 \lambda \\
 &\quad + a_z^2 \sin^2 \theta)(a_x^2 \sin^2 \lambda + a_y^2 \cos^2 \lambda) \\
 &\quad - (a_y^2 - a_x^2)^2 \cos^2 \theta \sin^2 \lambda \cos^2 \lambda, \\
 B &= \frac{-a_x a_y a_z}{q_n} (a_x^2 \cos^2 \theta \cos^2 \lambda + a_y^2 \cos^2 \theta \sin^2 \lambda \\
 &\quad + a_z^2 \sin^2 \theta + a_x^2 \sin^2 \lambda + a_y^2 \cos^2 \lambda), \\
 C &= (a_x a_y a_z / q_n)^2,
 \end{aligned} \tag{D.3}$$

in which

$$q_n = (a_y^2 a_z^2 \sin^2 \theta \cos^2 \lambda + a_x^2 a_z^2 \sin^2 \theta \sin^2 \lambda + a_x^2 a_y^2 \cos^2 \theta)^{1/2}.$$

A singularity in equation D.1 at $\theta = 0$ has been addressed analytically in equation D.2. The maximum and minimum radii of curvature at P are

$$\rho_{\max} = 1/\kappa_{\min}, \quad \rho_{\min} = 1/\kappa_{\max}.$$

REFERENCES

- Amoruso, A. & Crescentini, L., 2009. Shape and volume change of pressurized ellipsoidal cavities from deformation and seismic data, *Journal of Geophysical Research: Solid Earth*, **114**(B2).
- Amoruso, A. & Crescentini, L., 2011. Modelling deformation due to a pressurized ellipsoidal cavity, with reference to the campi flegrei caldera, italy, *Geophysical Research Letters*, **38**(1).
- Amoruso, A. & Crescentini, L., 2013. Analytical models of volcanic ellipsoidal expansion sources, *Annals of Geophysics*, **56**(4), 0435.
- Amoruso, A., Crescentini, L., Linde, A. T., Sacks, I. S., Scarpa, R., & Romano, P., 2007. A horizontal crack in a layered structure satisfies deformation for the 2004–2006 uplift of Campi Flegrei, *Geophysical Research Letters*, **34**(22).
- Amoruso, A., Crescentini, L., & Berrino, G., 2008. Simultaneous inversion of deformation and gravity changes in a horizontally layered half-space: evidences for magma intrusion during the 1982–1984 unrest at Campi Flegrei caldera (Italy), *Earth and Planetary Science Letters*, **272**(1-2), 181–188.
- Amoruso, A., Crescentini, L., & Sabetta, I., 2014. Paired deformation sources of the Campi Flegrei caldera (Italy) required by recent (1980-2010) deformation history, *Journal of Geophysical Research: Solid Earth*, **119**(2), 858–879.
- Anderson, K. & Segall, P., 2011. Physics-based models of ground deformation and extrusion rate at effusively erupting volcanoes, *Journal of Geophysical Research: Solid Earth*, **116**(B7).

- 620 Anderson, K. & Segall, P., 2013. Bayesian inversion of data from effusive volcanic eruptions using physics-
621 based models: Application to Mount St. Helens 2004–2008, *Journal of Geophysical Research: Solid Earth*,
622 **118**(5), 2017–2037.
- 623 Anderson, K. R. & Poland, M. P., 2016. Bayesian estimation of magma supply, storage, and eruption rates
624 using a multiphysical volcano model: Kīlauea volcano, 2000–2012, *Earth and Planetary Science Letters*,
625 **447**, 161–171.
- 626 Bagnardi, M. & Hooper, A., 2018. Inversion of Surface Deformation Data for Rapid Estimates of Source
627 Parameters and Uncertainties: A Bayesian Approach, *Geochemistry, Geophysics, Geosystems*, **19**(7), 2194–
628 2211.
- 629 Bato, M. G., Pinel, V., & Yan, Y., 2017. Assimilation of Deformation Data for Eruption Forecasting: Potent-
630 tiality Assessment Based on Synthetic Cases, *Frontiers in Earth Science*, **5**.
- 631 Battaglia, M., Cervelli, P. F., & Murray, J. R., 2013. dMODELS: A MATLAB software package for modeling
632 crustal deformation near active faults and volcanic centers, *Journal of Volcanology and Geothermal Research*,
633 **254**, 1–4.
- 634 Beauducel, F., Lafon, D., Béguin, X., Saurel, J.-M., Bosson, A., Mallarino, D., Boissier, P., Brunet, C., Lemarc-
635 hand, A., Anténor-Habazac, C., Necessian, A., & Fahmi, A. A., 2020a. Webobs: The volcano observatories
636 missing link between research and real-time monitoring, *Frontiers in Earth Science*, **8**.
- 637 Beauducel, F., Peltier, A., Villié, A., & Suryanto, W., 2020b. Mechanical imaging of a volcano plumbing
638 system from GNSS unsupervised modeling, *Geophysical Research Letters*, **47**(17), e2020GL089419.
- 639 Biggs, J. & Pritchard, M. E., 2017. Global Volcano Monitoring: What Does It Mean When Volcanoes Deform?,
640 *Elements*, **13**(1), 17–22.
- 641 Bonafede, M. & Ferrari, C., 2009. Analytical models of deformation and residual gravity changes due to a
642 Mogi source in a viscoelastic medium, *Tectonophysics*, **471**(1-2), 4–13.
- 643 Bruno, V., Aloisi, M., Gambino, S., Mattia, M., Ferlito, C., & Rossi, M., 2022. The Most Intense Deflation of
644 the Last Two Decades at Mt. Etna: The 2019-2021 Evolution of Ground Deformation and Modeled Pressure
645 Sources, *Geophysical Research Letters*, **49**(6), e2021GL095195.
- 646 Cannavó, F., 2019. A new user-friendly tool for rapid modelling of ground deformation, *Computers & Geo-
647 sciences*, **128**, 60–69.
- 648 Caricchi, L., Townsend, M., Rivalta, E., & Namiki, A., 2021. The build-up and triggers of volcanic eruptions,
649 *Nature Reviews Earth & Environment*, **2**(7), 458–476.
- 650 Carlson, B. C., 1995. Numerical computation of real or complex elliptic integrals, *Numerical Algorithms*,
651 **10**(1), 13–26.
- 652 Cervelli, P. F., 2013. Analytical expressions for deformation from an arbitrarily oriented spheroid in a half-
653 space, in *AGU Fall Meeting Abstracts*, vol. 2013, pp. V44C–06.
- 654 Cesca, S., Letort, J., Razafindrakoto, H. N., Heimann, S., Rivalta, E., Isken, M. P., Nikkhoo, M., Passarelli, L.,
655 Petersen, G. M., Cotton, F., & Dahm, T., 2020. Drainage of a deep magma reservoir near Mayotte inferred
656 from seismicity and deformation, *Nature Geoscience*, **13**(1), 87–93.

- 657 Comninou, M. & Dundurs, J., 1975. The angular dislocation in a half space, *Journal of Elasticity*, **5**(3–4),
658 203–216.
- 659 Crouch, S. L., 1976. Solution of plane elasticity problems by the displacement discontinuity method. I. Infinite
660 body solution, *International Journal for Numerical Methods in Engineering*, **10**(2), 301–343.
- 661 Crouch, S. L. & Starfield, A. M., 1983. *Boundary Element Method in Solid Mechanics*, Allen and Unwin,
662 London.
- 663 Davis, P., Hastie, L., & Stacey, F., 1974. Stresses within an active volcano—with particular reference to
664 Kilauea, *Tectonophysics*, **22**(3-4), 355–362.
- 665 Davis, P. M., 1983. Surface deformation associated with a dipping hydrofracture, *Journal of Geophysical*
666 *Research: Solid Earth*, **88**(B7), 5826–5834.
- 667 Davis, P. M., 1986. Surface deformation due to inflation of an arbitrarily oriented triaxial ellipsoidal cavity
668 in an elastic half-space, with reference to Kilauea volcano, Hawaii, *Journal of Geophysical Research: Solid*
669 *Earth*, **91**(B7), 7429–7438.
- 670 Davis, T., Bagnardi, M., Lundgren, P., & Rivalta, E., 2021. Extreme Curvature of Shallow Magma Pathways
671 Controlled by Competing Stresses: Insights From the 2018 Sierra Negra Eruption, *Geophysical Research*
672 *Letters*, **48**(13), e2021GL093038, e2021GL093038 2021GL093038.
- 673 Degruyter, W., Parmigiani, A., Huber, C., & Bachmann, O., 2019. How do volatiles escape their shallow mag-
674 matic hearth?, *Philosophical Transactions of the Royal Society A: Mathematical, Physical and Engineering*
675 *Sciences*, **377**(2139), 20180017.
- 676 Dumont, S., Sigmundsson, F., Parks, M. M., Drouin, V. J. P., Pedersen, G. B. M., Jónsdóttir, I., Höskuldsson,
677 Á., Hooper, A., Spaans, K., Bagnardi, M., Gudmundsson, M. T., Barsotti, S., Jónsdóttir, K., Högnadóttir, T.,
678 Magnússon, E., Hjartardóttir, Á. R., Dürig, T., Rossi, C., & Oddsson, B., 2018. Integration of SAR Data Into
679 Monitoring of the 2014-2015 Holuhraun Eruption, Iceland: Contribution of the Icelandic Volcanoes Supersite
680 and the FutureVolc Projects, *Frontiers in Earth Science*, **6**.
- 681 Dvorak, J. J. & Dzurlisin, D., 1997. Volcano geodesy: The search for magma reservoirs and the formation of
682 eruptive vents, *Reviews of Geophysics*, **35**(3), 343–384.
- 683 Dzurlisin, D., 2000. Volcano geodesy: challenges and opportunities for the 21st century, *Philosophical Transac-*
684 *tions of the Royal Society of London. Series A: Mathematical, Physical and Engineering Sciences*, **358**(1770),
685 1547–1566.
- 686 Dzurlisin, D., 2003. A comprehensive approach to monitoring volcano deformation as a window on the eruption
687 cycle, *Reviews of Geophysics*, **41**(1).
- 688 Dzurlisin, D., 2006. *Volcano deformation: new geodetic monitoring techniques*, Springer Science & Business
689 Media.
- 690 Edmonds, M. & Woods, A. W., 2018. Exsolved volatiles in magma reservoirs, *Journal of Volcanology and*
691 *Geothermal Research*, **368**, 13–30.
- 692 Eshelby, J. D., 1957. The determination of the elastic field of an ellipsoidal inclusion, and related problems,
693 *Proceedings of the royal society of London. Series A. Mathematical and physical sciences*, **241**(1226), 376–

- 694 396.
- 695 Fialko, Y., Khazan, Y., & Simons, M., 2001. Deformation due to a pressurized horizontal circular crack in
696 an elastic half-space, with applications to volcano geodesy, *Geophysical Journal International*, **146**(1), 181–
697 190.
- 698 Furuya, M., 2004. Localized deformation at miyakejima volcano based on jers-1 radar interferometry:
699 1992–1998, *Geophysical Research Letters*, **31**(5).
- 700 Furuya, M., 2005. Quasi-static thermoelastic deformation in an elastic half-space: theory and application to
701 InSAR observations at Izu-Oshima volcano, Japan, *Geophysical Journal International*, **161**(1), 230–242.
- 702 Harris, J. W. & Stöcker, H., 1998. *Handbook of mathematics and computational science*, Springer Science &
703 Business Media.
- 704 Heimann, S., Vasyura-Bathke, H., Sudhaus, H., Isken, M. P., Kriegerowski, M., Steinberg, A., & Dahm, T.,
705 2019. A Python framework for efficient use of pre-computed Green's functions in seismological and other
706 physical forward and inverse source problems, *Solid Earth*, **10**(6), 1921–1935.
- 707 Hill, D., Montgomery-Brown, E., Shelly, D., Flinders, A., & Prejean, S., 2020. Post-1978 tumescence at Long
708 Valley Caldera, California: A geophysical perspective, *Journal of Volcanology and Geothermal Research*,
709 **400**, 106900.
- 710 Kern, W. F. & Bland, J. R., 1938. *Solid mensuration: with proofs*, J. Wiley & Sons, Incorporated.
- 711 Klein, P. P., 2012. On the ellipsoid and plane intersection equation, *Applied Mathematics*, **3**(11), 1634–1640.
- 712 Kobayashi, T., Morishita, Y., & Munekane, H., 2018. First detection of precursory ground inflation of a small
713 phreatic eruption by InSAR, *Earth and Planetary Science Letters*, **491**, 244–254.
- 714 Kuriyama, K. & Mizuta, Y., 1993. Three-dimensional elastic analysis by the displacement discontinuity
715 method with boundary division into triangular leaf elements, *International Journal of Rock Mechanics and*
716 *Mining Sciences & Geomechanics Abstracts*, **30**(2), 111–123.
- 717 Langbein, J., Dzurisin, D., Marshall, G., Stein, R., & Rundle, J., 1995. Shallow and peripheral volcanic
718 sources of inflation revealed by modeling two-color geodimeter and leveling data from Long Valley Caldera,
719 California, 1988–1992, *Journal of Geophysical Research: Solid Earth*, **100**(B7), 12487–12495.
- 720 Lipschutz, M. M., 1969. *Schaum's outline of theory and problems of differential geometry*, McGraw-Hill, New
721 York.
- 722 Lisowski, M., 2007. *Analytical volcano deformation source models*, pp. 279–304, Springer Berlin Heidelberg,
723 Berlin, Heidelberg.
- 724 Lisowski, M., Dzurisin, D., Denlinger, R. P., & Iwatsubo, E. Y., 2008. Analysis of GPS-measured deforma-
725 tion associated with the 2004–2006 dome-building eruption of Mount St. Helens, Washington, in *A Volcano*
726 *Rekindled: The Renewed Eruption of Mount St. Helens, 2004–2006*, vol. 1750, pp. 301–333, US Geological
727 Survey Reston, Virginia.
- 728 Lisowski, M., McCaffrey, R., Wicks, C. W., & Dzurisin, D., 2021. Geodetic Constraints on a 25-year Mag-
729 matic Inflation Episode Near Three Sisters, Central Oregon, *Journal of Geophysical Research: Solid Earth*,
730 **126**(12), e2021JB022360, e2021JB022360 2021JB022360.

28 *Mehdi Nikkhoo, Eleonora Rivalta*

- Lu, Z. & Dzurisin, D., 2014. *Role of Ground Surface Deformation in Volcano Monitoring*, pp. 71–85, Springer Berlin Heidelberg, Berlin, Heidelberg.
- Mastin, L. G., Roeloffs, E., Beeler, N. M., & Quick, J. E., 2008. Constraints on the size, overpressure, and volatile content of the Mount St. Helens magma system from geodetic and dome-growth measurements during the 2004-2006+ eruption, Tech. rep., US Geological Survey.
- McTigue, D., 1987. Elastic stress and deformation near a finite spherical magma body: resolution of the point source paradox, *Journal of Geophysical Research: Solid Earth*, **92**(B12), 12931–12940.
- Mindlin, R. D., 1936. Force at a point in the interior of a semi-infinite solid, *physics*, **7**(5), 195–202.
- Mogi, K., 1958. Relations between the eruptions of various volcanoes and the deformations of the ground surfaces around them, *Earthq Res Inst*, **36**, 99–134.
- Narita, S., Murakami, M., & Tanaka, R., 2019. Quantitative relationship between plume emission and multiple deflations after the 2014 phreatic eruption at Ontake volcano, Japan, *Earth, Planets and Space*, **71**(145), 1–16.
- Narita, S., Ozawa, T., Aoki, Y., Shimada, M., Furuya, M., Takada, Y., & Murakami, M., 2020. Precursory ground deformation of the 2018 phreatic eruption on Iwo-Yama volcano, revealed by four-dimensional joint analysis of airborne and spaceborne InSAR, *Earth, Planets and Space*, **72**(145), 1–16.
- Nikkhoo, M. & Rivalta, E., 2022. Analytical Solutions for Gravity Changes Caused by Triaxial Volumetric Sources, *Geophysical Research Letters*, **49**(8), e2021GL095442, e2021GL095442 2021GL095442.
- Nikkhoo, M. & Walter, T. R., 2015. Triangular dislocation: an analytical, artefact-free solution, *Geophysical Journal International*, **201**(2), 1119–1141.
- Nikkhoo, M., Walter, T. R., Lundgren, P. R., & Prats-Iraola, P., 2017. Compound dislocation models (CDMs) for volcano deformation analyses, *Geophysical Journal International*, **208**(2), 877–894.
- Okada, Y., 1985. Surface deformation due to shear and tensile faults in a half-space, *Bulletin of the seismological society of America*, **75**(4), 1135–1154.
- Okubo, S., 1991. Potential and gravity changes raised by point dislocations, *Geophysical journal international*, **105**(3), 573–586.
- Peltier, A., Ferrazzini, V., Di Muro, A., Kowalski, P., Villeneuve, N., Richter, N., Chevrel, O., Froger, J. L., Hrysiewicz, A., Gouhier, M., Coppola, D., Retailleau, L., Beauducel, F., Gurioli, L., Boissier, P., Brunet, C., Catherine, P., Fontaine, F., Lauret, F., Garavaglia, L., Lebreton, J., Canjamale, K., Desfete, N., Griot, C., Harris, A., Arellano, S., Liuzzo, M., Gurrieri, S., & Ramsey, M., 2020. Volcano Crisis Management at Piton de la Fournaise (La Réunion) during the COVID-19 Lockdown, *Seismological Research Letters*, **92**(1), 38–52.
- Pinel, V., Poland, M., & Hooper, A., 2014. Volcanology: Lessons learned from Synthetic Aperture Radar imagery, *Journal of Volcanology and Geothermal Research*, **289**, 81–113.
- Poland, M. P. & Zebker, H. A., 2022. Volcano geodesy using InSAR in 2020: the past and next decades, *Bulletin of Volcanology*, **84**(27).
- Rivalta, E. & Segall, P., 2008. Magma compressibility and the missing source for some dike intrusions, *Geophysical Research Letters*, **35**(4).

- Salzer, J. T., Nikkhoo, M., Walter, T. R., Sudhaus, H., Reyes-Dávila, G., Bretón, M., & Arámbula, R., 2014. Satellite radar data reveal short-term pre-explosive displacements and a complex conduit system at volcán de Colima, Mexico, *Frontiers in Earth Science*, **2**.
- Segall, P., 2010. *Earthquake and volcano deformation*, Princeton University Press.
- Segall, P., 2016. Re-pressurization following eruption from a magma chamber with a viscoelastic aureole, *Journal of Geophysical Research: Solid Earth*, **121**(12), 8501–8522.
- Segall, P., Cervelli, P., Owen, S., Lisowski, M., & Miklius, A., 2001. Constraints on dike propagation from continuous GPS measurements, *Journal of Geophysical Research: Solid Earth*, **106**(B9), 19301–19317.
- Sigmundsson, F., Hooper, A., Hreinsdóttir, S., Vogfjörð, K. S., Ófeigsson, B. G., Heimisson, E. R., Dumont, S., Parks, M., Spaans, K., Gudmundsson, G. B., et al., 2015. Segmented lateral dyke growth in a rifting event at Bárðarbunga volcanic system, Iceland, *Nature*, **517**(7533), 191–195.
- Sun, R. J., 1969. Theoretical size of hydraulically induced horizontal fractures and corresponding surface uplift in an idealized medium, *Journal of Geophysical Research (1896-1977)*, **74**(25), 5995–6011.
- Trasatti, E., 2022. Volcanic and seismic source modeling: An open tool for geodetic data modeling, *Frontiers in Earth Science*, **10**.
- Trasatti, E., Acocella, V., Di Vito, M. A., Del Gaudio, C., Weber, G., Aquino, I., Caliro, S., Chiodini, G., de Vita, S., Ricco, C., & Caricchi, L., 2019. Magma Degassing as a Source of Long-Term Seismicity at Volcanoes: The Ischia Island (Italy) Case, *Geophysical Research Letters*, **46**(24), 14421–14429.
- Ueda, H., Nagai, M., & Tanada, T., 2018. Phreatic eruptions and deformation of Ioto Island (Iwo-jima), Japan, triggered by deep magma injection, *Earth, Planets and Space*, **70**(38), 1–15.
- Vasyura-Bathke, H., Dettmer, J., Steinberg, A., Heimann, S., Isken, M. P., Zielke, O., Mai, P. M., Sudhaus, H., & Jónsson, S., 2019. Beat: Bayesian earthquake analysis tool, Tech. rep.
- Vasyura-Bathke, H., Dettmer, J., Steinberg, A., Heimann, S., Isken, M. P., Zielke, O., Mai, P. M., Sudhaus, H., & Jónsson, S., 2020. The Bayesian earthquake analysis tool, *Seismological Research Letters*, **91**(2A), 1003–1018.
- Wang, R., Lorenzo-Martin, F., & Roth, F., 2006. PSGRN/PSCMP—a new code for calculating co- and post-seismic deformation, geoid and gravity changes based on the viscoelastic-gravitational dislocation theory, *Computers & Geosciences*, **32**(4), 527–541.
- Wang, T., Shi, Q., Nikkhoo, M., Wei, S., Barbot, S., Dreger, D., Bürgmann, R., Motagh, M., & Chen, Q.-F., 2018. The rise, collapse, and compaction of Mt. Mantap from the 3 September 2017 North Korean nuclear test, *Science*, **361**(6398), 166–170.
- Wang, X. & Aoki, Y., 2019. Post-eruptive thermoelastic deflation of intruded magma in Usu volcano, Japan, 1992–2017, *Journal of Geophysical Research: Solid Earth*, **124**(1), 335–357.
- Wasser, V. K., Lopez, T. M., Anderson, K. R., Izbekov, P. E., & Freymueller, J. T., 2021. Multidisciplinary Constraints on Magma Compressibility, the Pre-Eruptive Exsolved Volatile Fraction, and the H₂O/CO₂ Molar Ratio for the 2006 Augustine Eruption, Alaska, *Geochemistry, Geophysics, Geosystems*, **22**(9), e2021GC009911.

30 *Mehdi Nikkhoo, Eleonora Rivalta*

805 Wicks, C. W., Dzurisin, D., Lowenstern, J. B., & Svarc, J., 2020. Magma Intrusion and Volatile Ascent
806 Beneath Norris Geyser Basin, Yellowstone National Park, *Journal of Geophysical Research: Solid Earth*,
807 **125**(2), e2019JB018208, e2019JB018208 2019JB018208.

808 Xu, W., Jónsson, S., Corbi, F., & Rivalta, E., 2016. Graben formation and dike arrest during the 2009 Harrat
809 Lunayyir dike intrusion in Saudi Arabia: Insights from InSAR, stress calculations and analog experiments,
810 *Journal of Geophysical Research: Solid Earth*, **121**(4), 2837–2851.

811 Xu, W., Xie, L., Aoki, Y., Rivalta, E., & Jónsson, S., 2020. Volcano-wide deformation after the 2017 erta ale
812 dike intrusion, ethiopia, observed with radar interferometry, *Journal of Geophysical Research: Solid Earth*,
813 **125**(8), e2020JB019562.

814 Yang, X.-M., Davis, P. M., & Dieterich, J. H., 1988. Deformation from inflation of a dipping finite prolate
815 spheroid in an elastic half-space as a model for volcanic stressing, *Journal of Geophysical Research: Solid*
816 *Earth*, **93**(B5), 4249–4257.

817 Yoffe, E. H., 1960. The angular dislocation, *Philosophical Magazine*, **5**(50), 161–175.

818 Yunjun, Z., Amelung, F., & Aoki, Y., 2021. Imaging the Hydrothermal System of Kirishima Volcanic Complex
819 With L-Band InSAR Time Series, *Geophysical Research Letters*, **48**(11), e2021GL092879, e2021GL092879
820 2021GL092879.

821 Zhan, Y., Gregg, P. M., Chaussard, E., & Aoki, Y., 2017. Sequential Assimilation of Volcanic Monitoring Data
822 to Quantify Eruption Potential: Application to Kerinci Volcano, Sumatra, *Frontiers in Earth Science*, **5**.

823 This paper has been produced using the Blackwell Scientific Publications GJI L^AT_EX2e class file.

Geophys. J. Int. (0000) **000**, 000–000

Supplementary Information

Mehdi Nikkhoo^{1,2} and Eleonora Rivalta^{1,3}

¹ GFZ German Research Centre for Geosciences, Potsdam, Germany. E-mail: mehdi.nikkhoo@gfz-potsdam.de

² The Abdus Salam International Center for Theoretical Physics, Trieste, Italy,

³ Department of Physics and Astronomy, Alma Mater Studiorum University of Bologna, Italy.

Comparisons using the BEM solutions

We compared the surface displacements and volume changes calculated from the finite ECM and BEM for 114 triaxial ellipsoidal cavities (see Table S1). The number of TDs forming the cavities (except “Y1” and “Y2”, last two lines in Table S1) varies between 792 and 1984, with an average of 1138; the shallower and larger cavities possess more TDs. The cavity mesh in the “Y1” and “Y2” models is composed of 2456 and 4092 TDs, respectively—these models represent the same source and were used for a convergence test. Based on similar tests, we estimate a relative error of up to a few per cent for both the surface displacements and volume changes calculated using the BEM.

Table S1: Numerical benchmarking of the finite ECM using the BEM solutions. The semiaxes, a_x , a_y , a_z , and depth, d_C , of the cavities have the same arbitrary unit; the rotation angles, ω_x and ω_y , are given in degrees. The mean horizontal and vertical misfits associated with normalization method I, ϵ_I^h and ϵ_I^v , respectively, and those associated with method II, ϵ_{II}^h , ϵ_{II}^v , and also the relative volume change misfit, $\epsilon_{\delta V}$, are given in per cent (see section 3).

#	a_x	a_y	a_z	d_C	ω_x	ω_y	ϵ_I^h	ϵ_I^v	ϵ_{II}^h	ϵ_{II}^v	$\epsilon_{\delta V}$	$\frac{d_C}{a_C}$	$\frac{d_T}{a_C}$	$\frac{d_T}{\rho_{\max}}$	$\frac{d_T}{\rho_{\min}}$
A1	0.6	0.4	1.2	1.5	0	0	7.7	11	9.9	7.4	7.8	1.25	0.25	1	2.25
A2	0.6	0.4	1.2	1.8	0	0	6.0	7.8	3.8	3.6	6.3	1.5	0.5	2	4.5
A3	0.6	0.4	1.2	2.4	0	0	5.2	6.2	3.2	2.7	5.4	2.0	1.0	4	9
A4	0.6	0.4	1.2	3.0	0	0	5.0	5.7	3.2	2.6	5.1	2.5	1.5	6	14
A5	0.6	0.4	1.2	3.6	0	0	4.8	5.5	3.2	2.5	5.0	3.0	2.0	8	18
B1	0.3	0.2	1.2	1.5	0	0	6.2	7.1	4.1	3.5	5.4	1.25	0.25	4	9
B2	0.3	0.2	1.2	1.8	0	0	5.8	6.4	4.2	3.4	5.1	1.5	0.5	8	18
B3	0.3	0.2	1.2	2.4	0	0	5.6	6.0	4.2	3.4	4.8	2.0	1.0	16	36
B4	0.3	0.2	1.2	3.0	0	0	5.6	6.0	4.2	3.5	4.8	2.5	1.5	24	54
B5	0.3	0.2	1.2	3.6	0	0	5.5	5.9	4.2	3.4	4.8	3.0	2.0	32	72
C1	0.1	1.2	1.2	1.5	0	0	9.8	12	1.9	4.6	8.4	1.25	0.25	0.25	36
C2	0.1	1.2	1.2	1.8	0	0	6.0	7.9	1.3	3.3	6.1	1.5	0.5	0.5	72
C3	0.1	1.2	1.2	2.4	0	0	4.0	5.9	1.1	2.7	4.5	2.0	1.0	1	140
C4	0.1	1.2	1.2	3.0	0	0	3.3	5.2	1.0	2.6	4.0	2.5	1.5	1.5	220
C5	0.1	1.2	1.2	3.6	0	0	3.2	5.1	1.1	2.4	3.8	3.0	2.0	2	290
D0	1.5	1.2	0.1	0.9	0	0	45	46	11	7.3	77	0.6	0.53	0.036	0.056
D1	1.5	1.2	0.1	1.5	0	0	20	21	2.3	1.3	25	1.0	0.93	0.062	0.097
D2	1.5	1.2	0.1	1.8	0	0	14	15	1.2	0.6	17	1.2	1.1	0.076	0.12
D3	1.5	1.2	0.1	2.4	0	0	8.1	8.3	0.5	0.3	9.2	1.6	1.5	0.10	0.16
D4	1.5	1.2	0.1	3.0	0	0	5.0	5.2	0.4	0.2	5.9	2.0	1.9	0.13	0.20
D5	1.5	1.2	0.1	3.6	0	0	3.7	3.8	0.4	0.1	4.3	2.4	2.3	0.16	0.24
J0	1.5	0.3	0.3	0.9	0	0	9.4	12	7.1	4.1	11	0.6	0.4	0.08	2
J1	1.5	0.3	0.3	1.2	0	0	6.5	7.5	3.4	2.0	8.0	0.8	0.6	0.12	3
J2	1.5	0.3	0.3	1.5	0	0	5.0	5.5	1.6	1.0	6.6	1.0	0.8	0.16	4
J3	1.5	0.3	0.3	1.8	0	0	4.2	4.4	0.9	0.5	5.9	1.2	1.0	0.20	5
J5	1.5	0.3	0.3	2.4	0	0	3.5	3.5	0.7	0.2	5.3	1.6	1.4	0.28	7
J6	1.5	0.3	0.3	2.7	0	0	3.3	3.2	0.6	0.3	5.2	1.8	1.6	0.32	8
J7	1.5	0.3	0.3	3.0	0	0	3.0	3.0	0.6	0.3	5.1	2.0	1.8	0.36	9
K1	0.6	0.4	1.2	1.5	0	-10	7.7	11	10	7.3	7.8	1.3	0.26	1.0	2.3
K2	0.6	0.4	1.2	1.5	0	-20	7.6	11	11	7.3	7.8	1.3	0.29	1.0	2.5
K3	0.6	0.4	1.2	1.5	0	-30	7.8	11	11	7.2	7.7	1.3	0.35	1.0	2.8
K4	0.6	0.4	1.2	1.5	0	-40	7.9	11	10	6.4	7.7	1.3	0.42	0.96	3.1
K5	0.6	0.4	1.2	1.5	0	-50	8.0	11	8.7	5.5	7.7	1.3	0.50	0.84	3.4

2 Mehdi Nikkhoo, Eleonora Rivalta

Continuation of Table S1

#	a_x	a_y	a_z	d_C	ω_x	ω_y	ϵ_H^I	ϵ_V^I	ϵ_H^{II}	ϵ_V^{II}	$\epsilon_{\delta V}$	$\frac{d_C}{a_C}$	$\frac{d_T}{a_C}$	$\frac{d_T}{\rho_{max}}$	$\frac{d_T}{\rho_{min}}$
K6	0.6	0.4	1.2	1.5	0	-60	8.1	10	7.9	5.0	7.7	1.3	0.59	0.68	3.5
K7	0.6	0.4	1.2	1.5	0	-70	7.9	9.9	7.0	4.5	7.7	1.3	0.67	0.53	3.5
K8	0.6	0.4	1.2	1.5	0	-80	7.9	9.7	6.9	4.5	7.7	1.3	0.73	0.41	3.4
K9	0.6	0.4	1.2	1.5	0	-90	7.7	9.5	6.7	4.5	7.7	1.3	0.75	0.38	3.4
L1	0.6	0.4	1.2	1.5	-10	0	8.0	11	8.1	6.1	8.0	1.3	0.26	1.0	2.3
L2	0.6	0.4	1.2	1.5	-20	0	8.0	10	7.3	5.2	8.3	1.3	0.30	1.2	2.3
L3	0.6	0.4	1.2	1.5	-30	0	7.9	9.8	6.5	4.6	8.9	1.3	0.37	1.3	2.3
L4	0.6	0.4	1.2	1.5	-40	0	7.8	9.5	5.9	4.1	9.5	1.3	0.46	1.5	2.1
L5	0.6	0.4	1.2	1.5	-50	0	7.7	9.1	5.2	3.5	10	1.3	0.56	1.5	1.7
L6	0.6	0.4	1.2	1.5	-60	0	7.5	8.9	4.3	2.8	11	1.3	0.67	1.2	1.6
L7	0.6	0.4	1.2	1.5	-70	0	7.6	8.8	3.9	2.5	11	1.3	0.79	0.71	1.5
L8	0.6	0.4	1.2	1.5	-80	0	7.7	8.9	3.5	2.1	11	1.3	0.88	0.41	1.3
L9	0.6	0.4	1.2	1.5	-90	0	7.7	8.9	2.9	1.5	11	1.3	0.92	0.31	1.2
M1	0.6	0.4	1.2	1.8	0	-10	6.1	7.9	4.1	3.8	6.3	1.5	0.51	2.0	4.6
M2	0.6	0.4	1.2	1.8	0	-20	6.3	8.1	4.5	3.9	6.3	1.5	0.55	1.9	4.7
M3	0.6	0.4	1.2	1.8	0	-30	6.5	8.1	5.1	3.9	6.3	1.5	0.60	1.8	4.9
M4	0.6	0.4	1.2	1.8	0	-40	6.7	8.1	5.7	4.0	6.4	1.5	0.67	1.5	5.0
M5	0.6	0.4	1.2	1.8	0	-50	6.9	8.1	5.7	3.9	6.4	1.5	0.75	1.3	5.1
M6	0.6	0.4	1.2	1.8	0	-60	6.9	8.0	5.2	3.5	6.4	1.5	0.84	0.97	5.0
M7	0.6	0.4	1.2	1.8	0	-70	6.8	7.9	4.9	3.3	6.5	1.5	0.92	0.72	4.8
M8	0.6	0.4	1.2	1.8	0	-80	6.5	7.6	4.3	2.9	6.5	1.5	0.98	0.56	4.6
M9	0.6	0.4	1.2	1.8	0	-90	6.3	7.5	4.3	2.9	6.5	1.5	1.0	0.5	4.5
N1	0.6	0.4	1.2	1.8	-10	0	6.0	7.3	3.3	3.1	6.4	1.5	0.51	2.0	4.4
N2	0.6	0.4	1.2	1.8	-20	0	5.8	6.8	2.8	2.4	6.6	1.5	0.55	2.1	4.2
N3	0.6	0.4	1.2	1.8	-30	0	5.5	6.4	2.5	1.9	7.0	1.5	0.62	2.2	3.8
N4	0.6	0.4	1.2	1.8	-40	0	5.4	6.2	2.5	1.8	7.4	1.5	0.71	2.2	3.2
N5	0.6	0.4	1.2	1.8	-50	0	5.2	5.9	2.2	1.5	7.9	1.5	0.81	2.2	2.4
N6	0.6	0.4	1.2	1.8	-60	0	5.2	5.9	2.0	1.3	8.2	1.5	0.92	1.6	2.1
N7	0.6	0.4	1.2	1.8	-70	0	5.1	5.7	1.6	0.9	8.5	1.5	1.04	0.93	1.9
N8	0.6	0.4	1.2	1.8	-80	0	5.4	5.9	1.4	0.8	8.7	1.5	1.13	0.52	1.7
N9	0.6	0.4	1.2	1.8	-90	0	5.6	6.0	1.2	0.7	8.8	1.5	1.17	0.39	1.6
O1	0.6	0.4	1.2	2.1	-10	0	5.2	6.1	3.0	2.6	5.7	1.8	0.76	3.0	6.6
O2	0.6	0.4	1.2	2.1	-20	0	4.8	5.4	2.5	2.0	5.9	1.8	0.80	3.0	6.1
O3	0.6	0.4	1.2	2.1	-30	0	4.4	4.9	2.0	1.4	6.1	1.8	0.87	3.1	5.4
O4	0.6	0.4	1.2	2.1	-40	0	4.2	4.6	1.5	1.1	6.4	1.8	0.96	3.0	4.3
O5	0.6	0.4	1.2	2.1	-50	0	4.1	4.4	1.2	0.9	6.7	1.8	1.06	2.9	3.2
O6	0.6	0.4	1.2	2.1	-60	0	3.9	4.1	0.8	0.6	7.0	1.8	1.2	2.0	2.7
O7	0.6	0.4	1.2	2.1	-70	0	4.0	4.2	0.7	0.5	7.2	1.8	1.3	1.15	2.4
O8	0.6	0.4	1.2	2.1	-80	0	3.8	4.0	0.3	0.1	7.4	1.8	1.4	0.64	2.1
O9	0.6	0.4	1.2	2.1	-90	0	4.1	4.1	0.2	0.2	7.4	1.8	1.4	0.47	1.9
P0	1.5	1.5	0.1	0.9	0	0	52	53	14	8.9	100	0.6	0.53	0.036	0.036
P1	1.5	1.5	0.1	1.2	0	0	36	37	6.8	4.4	53	0.8	0.73	0.049	0.049
P2	1.5	1.5	0.1	1.5	0	0	25	25	3.2	2.0	33	1.0	0.93	0.062	0.062
P3	1.5	1.5	0.1	1.8	0	0	18	18	1.6	1.0	22	1.2	1.1	0.076	0.076
P4	1.5	1.5	0.1	2.1	0	0	13	13	0.6	0.4	16	1.4	1.3	0.089	0.089
P5	1.5	1.5	0.1	2.4	0	0	10	11	0.6	0.3	12	1.6	1.5	0.10	0.10
P6	1.5	1.5	0.1	2.7	0	0	7.8	8.0	0.4	0.2	9.3	1.8	1.7	0.12	0.12
P7	1.5	1.5	0.1	3	0	0	6.4	6.7	0.4	0.2	7.5	2.0	1.9	0.13	0.13
P8	1.5	1.5	0.1	3.3	0	0	4.9	5.2	0.8	0.6	6.3	2.2	2.1	0.14	0.14
P9	1.5	1.5	0.1	3.6	0	0	4.7	4.7	0.3	0.1	5.4	2.4	2.3	0.16	0.16
Q0	1.5	1.5	0.3	0.9	0	0	54	58	29	16	120	0.6	0.4	0.08	0.08
Q1	1.5	1.5	0.3	1.2	0	0	37	40	15	8.3	60	0.8	0.6	0.12	0.12
R1	0.6	0.4	1.2	2.1	0	-10	5.6	6.8	3.2	3.0	5.7	1.8	0.76	2.9	6.8
R2	0.6	0.4	1.2	2.1	0	-20	5.8	6.9	3.4	3.1	5.7	1.8	0.80	2.8	6.8
R3	0.6	0.4	1.2	2.1	0	-30	6.0	7.0	3.7	3.0	5.7	1.8	0.85	2.5	6.9
R4	0.6	0.4	1.2	2.1	0	-40	6.2	7.0	4.1	3.0	5.8	1.8	0.92	2.1	6.9
R5	0.6	0.4	1.2	2.1	0	-50	6.4	7.0	4.5	3.0	5.8	1.8	1.0	1.7	6.8
R6	0.6	0.4	1.2	2.1	0	-60	6.5	7.0	4.3	2.9	5.8	1.8	1.1	1.3	6.5
R7	0.6	0.4	1.2	2.1	0	-70	6.1	6.8	3.8	2.5	5.9	1.8	1.2	0.92	6.1
R8	0.6	0.4	1.2	2.1	0	-80	6.0	6.7	3.6	2.5	5.9	1.8	1.2	0.70	5.8

Supplementary Information: The finite ellipsoidal cavity model 3

Continuation of Table S1

#	a_x	a_y	a_z	d_C	ω_x	ω_y	ϵ_H^I	ϵ_V^I	ϵ_H^{II}	ϵ_V^{II}	$\epsilon_{\delta V}$	$\frac{d_C}{a_C}$	$\frac{d_T}{a_C}$	$\frac{d_T}{\rho_{\max}}$	$\frac{d_T}{\rho_{\min}}$
R9	0.6	0.4	1.2	2.1	0	-90	5.9	6.7	3.6	2.5	5.9	1.8	1.3	0.63	5.6
S1	0.6	0.4	1.2	2.4	0	-10	5.3	6.2	3.3	2.8	5.4	2.0	1.0	3.9	9.0
S2	0.6	0.4	1.2	2.4	0	-20	5.5	6.3	3.4	2.8	5.4	2.0	1.0	3.6	9.0
S3	0.6	0.4	1.2	2.4	0	-30	5.7	6.4	3.6	2.7	5.4	2.0	1.1	3.2	8.9
S4	0.6	0.4	1.2	2.4	0	-40	5.9	6.4	3.7	2.6	5.4	2.0	1.2	2.7	8.7
S5	0.6	0.4	1.2	2.4	0	-50	6.0	6.4	3.9	2.5	5.5	2.0	1.3	2.1	8.4
S6	0.6	0.4	1.2	2.4	0	-60	6.1	6.4	3.8	2.5	5.5	2.0	1.3	1.6	8.0
S7	0.6	0.4	1.2	2.4	0	-70	6.1	6.4	3.6	2.5	5.5	2.0	1.4	1.1	7.4
S8	0.6	0.4	1.2	2.4	0	-80	5.5	6.1	3.3	2.1	5.5	2.0	1.5	0.84	6.9
S9	0.6	0.4	1.2	2.4	0	-90	5.3	5.9	3.1	1.9	5.5	2.0	1.5	0.75	6.8
T1	0.6	0.4	1.2	2.4	-10	0	4.8	5.5	3.0	2.5	5.4	2.0	1.0	4.0	8.8
T2	0.6	0.4	1.2	2.4	-20	0	4.3	4.6	2.6	1.9	5.5	2.0	1.1	4.0	8.0
T3	0.6	0.4	1.2	2.4	-30	0	3.8	4.0	2.1	1.4	5.7	2.0	1.2	3.9	6.9
T4	0.6	0.4	1.2	2.4	-40	0	3.5	3.6	1.6	1.0	5.9	2.0	1.2	3.8	5.5
T5	0.6	0.4	1.2	2.4	-50	0	3.3	3.4	1.2	0.8	6.1	2.0	1.3	3.6	3.9
T6	0.6	0.4	1.2	2.4	-60	0	3.4	3.4	0.9	0.6	6.3	2.0	1.4	2.5	3.3
T7	0.6	0.4	1.2	2.4	-70	0	3.0	3.0	0.6	0.4	6.5	2.0	1.5	1.4	2.9
T8	0.6	0.4	1.2	2.4	-80	0	3.1	3.0	0.5	0.2	6.6	2.0	1.6	0.75	2.4
T9	0.6	0.4	1.2	2.4	-90	0	3.3	3.0	0.8	0.4	6.6	2.0	1.7	0.56	2.2
Y1	0.2	0.2	1.2	3.6	0	0	3.5	4.4	1.4	1.4	4.8	3.0	2.0	72	72
Y2	0.2	0.2	1.2	3.6	0	0	3.0	3.8	1.3	1.3	3.7	3.0	2.0	72	72

This paper has been produced using the Blackwell Scientific Publications GJI L^AT_EX2e class file.